Machine learning of Antarctic firn density by combining radiometer and scatterometer remote sensing data

Weiran Li [1], Sanne B. M. Veldhuijsen [3], and Stef Lhermitte [2, 1]

[1]Department of Geoscience and Remote Sensing, Delft University of Technology, Delft, The Netherlands
[2]Department of Earth & Environmental Sciences, KU Leuven, Leuven, Belgium
[3]Institute for Marine and Atmospheric research Utrecht (IMAU), Utrecht, The Netherlands

Correspondence: Weiran Li (w.li-7@tudelft.nl)

Abstract. Firn density plays a crucial role in assessing the surface mass balance of the Antarctic ice sheet. However, our understanding of the spatial and temporal variations in firn density is limited due to i) spatial and temporal limitations of in situ measurements, ii) potential modelling uncertainties, and iii) lack of firn density products driven by satellite remote sensing data. To address this gap, this paper explores the potential of satellite microwave radiometer (SMISS) and scatterometer (ASCAT) observations for assessing spatial and temporal dynamics of dry firn density over the Antarctic ice sheet. Our analysis demonstrates a clear relation between density anomalies at a depth of ~~12~~40 cm and fluctuations in satellite observations. However, a linear relationship with individual satellite observations is insufficient to explain the spatial and temporal variation of snow density. Hence, we investigate the potential of a non-linear Random Forest (RF) machine learning approach trained on radiometer and scatterometer data to derive the spatial and temporal variations in dry firn density. In the estimation process, ten years of SSMIS observations (brightness temperature) ~~,~~ and ASCAT observations (backscatter intensity) ~~, and polarisation and frequency ratios derived from SSMIS observations~~ are used as input features to a random forest (RF) regressor. The regressor is first trained on time series of modelled density and satellite observations at randomly sampled pixels, and then applied to estimate densities in dry firn areas across Antarctica. The RF results reveal a strong agreement between the spatial patterns estimated by the RF regressor and the modelled densities. The estimated densities exhibit an error of $\pm 10\ kg\ m^{-3}$ in the interior of the ice sheet and ~~$\pm 20\ kg\ m^{-3}$~~ $\pm 35\ kg\ m^{-3}$ towards the ocean. However, the temporal patterns show some discrepancies, as the RF regressor tends to overestimate summer densities, except for high-elevation regions in East Antarctica and specific areas in West Antarctica. These errors may be attributed to underestimations of short-term or seasonal variations in the modelled density and the limitation of RF in extrapolating values outside the training data. Overall, our study presents a potential method for estimating unknown Antarctic firn densities using known densities and satellite parameters.

1 Introduction

The accelerated loss of mass from the Antarctic Ice Sheet, a trend anticipated to persist in the coming decades and centuries, underscores Antarctica's pivotal role as a major source of uncertainty in projecting future sea level rise (Pattyn and Morlighem, 2020). Recognising the critical contribution to sea level rise uncertainty highlights the urgency of comprehending Antarctica's surface mass balance (SMB). A typical method to estimate SMB of the Antarctic ice sheet is to convert satellite altimetry height

measurements into SMB (Zwally et al., 2005; Kuipers Munneke et al., 2015; Schröder et al., 2019) with the help of firn (an intermediate state between snow and glacial ice; van den Broeke, 2008; Amory et al., 2024) density. In Antarctica, firn density is highly variable in space and time due to the varying surface climate conditions (Craven and Allison, 1998; Li and Zwally, 2004; van den Broeke, 2008; Fujita et al., 2016). Therefore, it is necessary to continuously monitor firn density in Antarctica.

A variety of methods has been developed to assess firn density. In situ measurements from firn cores, snow pits and local near-infrared pictures are precious for accurately understanding firn densities; however, these measurements are sparse in both space and time due to cost-efficiency considerations, making them insufficient for comprehensive monitoring requirements (Macelloni et al., 2007; Picard et al., 2012; Champollion et al., 2013). In the absence of in situ data, firn densification models (FDMs), such as the semi-empirical IMAU-FDM (Ligtenberg et al., 2011; Veldhuijsen et al., 2023) are commonly utilised to estimate firn density and subsequent elevation changes (Schröder et al., 2019). Nonetheless, FDMs suffer from significant uncertainties (Verjans et al., 2020). For instance, the relationship between wind velocity and density, as derived by Sugiyama et al. (2012) and van den Broeke et al. (1999) exhibits notable discrepancies, introducing uncertainties when ~~parameterising~~ parametrising the effects of wind. Therefore, to obtain spatially and temporally continuous assessments of changes in firn densities, satellite remote sensing serves as an important complementary method (Picard et al., 2007; Brucker et al., 2014; Meredith et al., 2019). While numerous studies have investigated these assessments, they have identified intricate relationships between remote sensing observations and firn density, making it challenging to generalise remote sensing models. Consequently, a satellite-based firn density product remains elusive.

Among satellite remote sensing techniques, radiometers are a primary tool used for studying firn properties, offering various frequencies and polarisations that facilitate assessments of different firn properties at different depths (Picard et al., 2007, 2012; Champollion et al., 2013; Brucker et al., 2014; Amory et al., 2024). Radiometers measure the thermal radiation emitted by the ground surface and subsurface within the range of microwave penetration (Picard et al., 2007) and typically have a spatial resolution of ~ 25 km. The observed parameter is referred to as brightness temperature (T_B), which has been typically used to derive Antarctic surface melting extent by detecting the sharp increase in emissivity and hence T_B (Picard et al., 2007; Tedesco, 2009; Nicolas et al., 2017; de Roda Husman et al., 2022). However, studies show that T_B can also be used to assess firn densities. For example, Champollion et al. (2013) used the temporal variation of polarisation ratio ~~(horizontal/vertical)~~ of T_B at 19 GHz and 37 GHz to evaluate the density changes of firn induced by hoar-crystal formation and disappearance ~~.~~ at Dome C (75.06° S, 123.21° E, indicated in Fig. 2a). Alternatively, Tran et al. (2008) classified seven firn facies over Antarctica using a combination of T_B, a specific ratio defined by T_B at 23.8 GHz and 36.5 GHz, and information from Ku- and S-band altimeters acquired in 2004. They attributed the different facies to varying surface roughness or firn grain size driven by differences in climate parameters such as wind patterns, firn accumulation, and temperature, which are known to influence firn density (Lehning et al., 2002; Champollion et al., 2013).

Alternatively, active microwave observations, specifically radar scatterometer and synthetic aperture radar (SAR) with spatial resolutions of ~ 25 km and up to ~ 5 m, respectively, have been used to assess firn properties. The backscatter intensity (σ^0) is a common parameter measured by both scatterometer and SAR. Numerous studies have been performed to link the spatial or temporal variation of σ^0 to variations of certain firn properties. Fraser et al. (2016) analysed the drivers of spatial variation

of C-band scatterometer σ^0 acquired between 2007 and 2012 in dry firn zones of Antarctica. Their study concluded that (i) the seasonal variation of σ^0 is primarily driven by precipitation and firn temperature cycles, and (ii) σ^0 exhibits a high correlation with long-term precipitation, ~~whereas densitiesdo not play a dominant role~~which also affects long-term densities. On the other hand, Rizzoli et al. (2017) exploited interferometric acquisitions of X-band SAR σ^0 from TanDEM-X, using the combination of σ^0 and a volume correlation factor to classify Greenland into four firn facies with an unsupervised machine learning method. The firn facies classified by this study can be attributed to different melt extents.

The aforementioned studies indicate the capability of various passive and active satellite observations, either individually or in combination, to evaluate spatial and temporal patterns of firn density. However, the precise mechanisms underlying the impact of firn density on satellite observations cannot always be fully understood (Champollion et al., 2013; Fraser et al., 2016; Rizzoli et al., 2017). In addition, previous studies using satellite observations to assess firn properties are either restricted to a specific location where in situ measurements are available (Champollion et al., 2013) or to a specific time period (Tran et al., 2008). Generalisation of these aforementioned approaches to other areas or time periods therefore requires further assessment. Hence, it is crucial to identify suitable combinations of satellite observations and data fusion methods that enable the assessment of firn density across extensive regions and multiple seasons.

Consequently, the objective of this study is to propose and assess a methodology to derive firn density and its spatial and temporal variations over the Antarctic ice sheet based on ~~on~~ daily satellite observations. To achieve this, we conduct a threefold experiment involving the comparison of time series data from Special Sensor Microwave Imager/Sounder (SSMIS) and Advanced Scatterometer (ASCAT) satellites with the output of a semi-empirical firn densification model (IMAU-FDM). In the first experiment, we juxtapose the satellite time series with the output of IMAU-FDM to evaluate the potential of individual satellite parameters in linearly explaining density variations. The second experiment involves clustering analysis on the combined SSMIS and ASCAT satellite data to identify spatial and temporal patterns of satellite observations and compare them with IMAU-FDM density patterns. Finally, we assess the potential of a non-linear Random Forest (RF) machine learning approach (Breiman, 1996, 2001) trained on SSMIS and ASCAT data to derive spatial and temporal variations in dry firn density. More specifically, assuming firn densities in certain regions are known, this experiment aims to estimate firn densities of the unknown regions in space and time using a combination of satellite observations. Due to the currently limited availability of in situ density measurements, however, our study uses part of the modelled IMAU-FDM densities as "known" densities to train the RF regressor. Finally, we evaluate our RF predictions with external reference data, i.e. available in situ firn density measurements (Surface Mass Balance and Snow on Sea Ice Working Group; SUMup) and ERA5 climate parameters.

2 Data

In this study, we evaluate the potential of satellite microwave radiometer (SMISS) and scatterometer (ASCAT) observations in assessing the spatial and temporal dynamics of dry firn density across the Antarctic ice sheet. We focus on the grounded Antarctic ice sheet only, where wet firn and melting that potentially affect the satellite microwave observations are less pronounced (Lenaerts et al., 2016; Kingslake et al., 2017; Spergel et al., 2021; Li et al., 2021; de Roda Husman et al., 2022). To

account for this, we mask out all satellite observations over the ice shelves using the grounding line defined by Depoorter et al. (2013).

2.1 Radiometer data

Time series of brightness temperature (T_B) from the Special Sensor Microwave Imager/Sounder (SSMIS) sensors are used in this study as they are widely used to assess variations in firn properties (Tedesco and Kim, 2006; Tran et al., 2008; Brucker et al., 2010). The available measurement channels include vertically and horizontally polarised 19 GHz, 37 GHz and 91.655 GHz, and vertically polarised 22 GHz (Kunkee et al., 2008). However, for the purposes of this study, our focus is solely on the 19 GHz and 37 GHz channels, since the atmospheric influence is negligible at these frequencies (Picard et al., 2009; Brucker et al., 2011; Champollion et al., 2013). Theoretically, the penetration depths are 1–7 m (at 19 GHz) and 0.1–2 m (at 37 GHz) in dry snow zones of Antarctica (Surdyk, 2002; Brucker et al., 2010). With the presence of liquid water, the imaginary part of snow permittivity increases, therefore T_B increases (Tedesco, 2007). However, the actual penetration depths can still vary per region (Picard et al., 2009). These characteristics ensure the possibility for SSMIS at 19 GHz and 37 GHz to monitor the changes of firn properties at a variety of depths. The daily polar-gridded T_B data are acquired from the National Snow and Ice Data Center (NSIDC) with a spatial resolution of ~~25~~ 25 km for both the ~~19 GHz and 37~~ 19 GHz and 37 GHz channels (Meier et al., 2021). All data are acquired by the F17 sensor as it provides continuous daily data acquisition in the period between Jan. 1, 2011 and Dec. 31, 2020.

~~Besides the 19 GHz and 37 GHz T_B time series, we also derive the polarisation ratio and gradient ratio as they have been found to be associated with firn properties (Tran et al., 2008; Champollion et al., 2013). The polarisation ratio $PR(f)$ and gradient ratio $FR(p)$ are defined as~~

$$PR(f) = \frac{T_B(f, \mathrm{V})}{T_B(f, \mathrm{H})}$$

$$FR(p) = \frac{T_B(19\ \mathrm{GHz}, p)}{T_B(37\ \mathrm{GHz}, p)}$$

~~where f corresponds to the 19 GHz or 37 GHz frequencies, respectively, and p corresponds to the different horizontal (H) an vertical (V) polarisations, respectively. We adopt $PR(f)$ as the H polarisation is more sensitive to the near-surface firn density and the surface roughness than the V polarisation (Leduc-Leballeur et al., 2017); and adopt $FR(p)$ as the snow emissivity at different frequencies has different sensitivity to scattering from the varying snow grain size, which potentially reveals the grain size variation (Brucker et al., 2010; Picard et al., 2012). It is important to note that we define $PR(f)$ inversely to Champollion et al. (2013), who took the ratio of H over V. Therefore, in regions with possible hoar crystals which correspond to a low density, our $PR(f)$ is expected to decrease instead of increase.~~

2.2 Scatterometer data

Backscatter intensity (σ^0) from synthetic aperture radar (SAR) was also previously used to assess density variations due to the melting–refreezing process of certain firn types (Rizzoli et al., 2017) and to examine variations in firn facies (Fahnestock et al., 1993). In this study, we employ time series of ~~σ^0~~ backscatter intensity from the Advanced Scatterometer (ASCAT) satellite sensor as an alternative to SAR σ^0, primarily due to its high temporal resolution (daily) and its coverage over the entire Antarctica. ASCAT is an operational C-band (5.255 GHz) fan-beam scatterometer (Figa-Saldaña et al., 2002; Fraser et al., 2016) that has been in operation on Metop satellites since 2006. It operates in V ~~polarization~~ polarisation and covers multiple incidence angles. For dry firn, penetration depth of C-band ASCAT is approximately 20 m ~~(Rignot, 2002; Fraser et al., 2016) .~~ (Rignot, 2002). However, the top 1 m is most exposed to atmospheric drivers, which also affect the variability of C-band microwave (Fraser et al., 2016). The ASCAT products used in this study are obtained from Brigham Young University (BYU) Microwave Earth Remote Sensing (MERS) laboratory (2010) (Long et al., 1993; Early and Long, 2001; Lindsley and Long, 2010). The data are processed using the scatterometer image reconstruction (SIR) algorithm, which enhances the spatial resolution of images from 25 km to 4.45 km. The ~~σ^0~~ backscattering product adopted in our study is referred to as the A product in Long and Drinkwater (2000):

$$\sigma^0(\theta) = A + B(\theta - 40^\circ) \tag{1}$$

where A (in dB) is the originally measured σ^0 normalised to 40°, and B (in $dB/^\circ$) is a parameter describing the dependence of the original σ^0 on θ. The processing of Long and Drinkwater (2000) accounts for the incidence angle dependence of the originally measured σ^0, as the measurements are made over multiple incidence angles (between 20° and 55°). In this study, we only use the isotropic, normalised A parameter (hereafter ~~σ^0~~ σ^0_A) as it has been shown to better correlate with various climate parameters as well as the long-term firn density (Fraser et al., 2016). In addition, the presence of liquid water can reduce the volume scattering and increase the microwave absorption (Stiles and Ulaby, 1980); this should be taken care of and will be elaborated in Sect. 3. To ensure consistent analysis between T_B and ~~σ^0~~ σ^0_A, the BYU ~~σ^0~~ σ^0_A products are interpolated to the same polar grids as the SSMIS T_B products using bi-linear interpolation. The data acquisition time is the same as that of the radiometer data.

2.3 Densities from Firn Densification Model

To understand the spatio-temporal variation in satellite data, we compare the SMISS and ASCAT satellite data to the output of a semi-empirical firn densification model. Therefore, we use output from the latest version of the IMAU Firn Densification Model (IMAU-FDM v1.2A; Veldhuijsen et al., 2023). IMAU-FDM simulates the transient evolution of the Antarctic firn column, and is forced at the upper boundary by outputs of the Regional Atmospheric Climate Model (RACMO2.3p2) at a 27 km horizontal resolution (van Wessem et al., 2018) and with a temporal resolution of 10 days. The model employs up to 300 layers in total of 3 to 15 cm thickness, which represent the firn properties in a Lagrangian way. The output is resampled to a regular grid with layers of 4 cm. The density of the freshly fallen snow is a function of instantaneous wind speed and

temperature in IMAU-FDM. Over time, the simulated firn layers become denser due to dry-snow densification and meltwater refreezing.

~~For the comparison with satellite observations, we focus on the density of the top 12 cm (ρ_{12cm}) from the~~ To estimate at which depth the firn density has impact on satellite microwave, we perform a correlation estimation between satellite observation time series and IMAU-FDM ~~output. We also use ρ_{12cm} for density estimation using the random forest (RF) regressor. The choice of the 12 cm depth is based on (i) the fact that many in situ measurements used for evaluating the density estimations have been acquired at depths that are several centimetres below the surface, e.g. Picard et al. (2012) and Leduc-Leballeur et al. (2017), and (ii) a compromise between the expected penetration depths at 19 GHz and 37 GHz (0.1–2 m; Surdyk, 2002).~~

density at different depths, as elaborated in Section 3.1. The unrealistically large values in ~~ρ_{12cm}~~ IMAU-FDM densities (more than ~~$1000\ kg\ m^{-3}$~~ $917\ kg\ m^{-3}$) are treated as invalid. To facilitate comparison with the satellite products, the firn density data from IMAU-FDM are ~~reprojected~~ re-projected using bi-linear interpolation to the same polar grids as the satellite data, where valid data are restricted to pixels within the Antarctica coastline provided by Depoorter et al. (2013).

2.4 Reference in situ density measurements

Furthermore, we employ in situ density measurements obtained from the SUMup dataset (Koenig and Montgomery, 2018; Montgomery et al., 2018) as a reference for spatial evaluation of the satellite data and the RF regressor. SUMup provides information on start-point, end-point and mid-point of measurements. We use the mid-point here to define the depth of the reference data. For each date of measurement at each location, if multiple measurements are available, only the density measurements at the shallowest mid-point depths are used. Such depths are also restricted to < 1 m. The measurements within the depth restriction were taken between Jan. 22, 1984 and Jan. 23, 2017, and consist of 67 valid points. The SUMup dataset does not contain time series, but only single measurements on specific irregular dates throughout the time period between 1984 and 2017. Therefore, we use the SUMup dataset only for spatial evaluation of the potential uncertainties from both the IMAU-FDM densities and the densities estimated by the RF regressor.

~~In addition to the spatial evaluation, a temporal comparison between the IMAU-FDM densities and in situ densities can be performed at Dome C (75.06° S, 123.21° E, indicated in Fig. 2a) using the dataset from Leduc-Leballeur et al. (2017) available at Leduc-Leballeur et al. (2021). The measurements were taken between Oct. 7, 2014 and Jun. 1, 2015 at the depth of $0 - 2$ cm. The discrete measurements are interpolated to create a continuous time series for visual analysis.~~

2.5 ERA5 climate parameters

As mentioned in Sect. 1, IMAU-FDM can introduce discrepancies due to simplified ~~parameterisation~~ parametrisation (Verjans et al., 2020), which can be propagated in the estimation process with the RF regressor. Therefore, to interpret the difference between the measured (SUMup or Leduc-Leballeur et al. (2017) data), modelled (IMAU-FDM) and estimated (RF) densities, it is important to understand the effects of climate conditions. Therefore, we use ERA5 wind speed ~~and surface temperature~~ estimated at midday (Copernicus Climate Change Service, 2019) as an approximation of the daily ~~weather~~ wind conditions. By

incorporating this information, we aim to better understand the discrepancies between the observed and IMAU-FDM densities, as well as the source of discrepancies between the IMAU-FDM densities and the densities estimated from satellite observations with the RF regressor. The ERA5 wind speed ~~and surface temperature~~ data have a horizontal resolution of 9 km. Similarly to the IMAU-FDM data, we interpolate these climate variables to the same polar grids as the SSMIS data using bi-linear interpolation to ensure consistency in the analysis.

3 Method

We ~~asses~~ assess the potential of SSMIS and ASCAT satellite observations to assess dry firn density in a three-fold experiment. First, we compare the satellite time series with the output of IMAU-FDM to evaluate the potential of individual satellite parameters to linearly explain density variations (Sect. 3.1). Second, we perform a clustering analysis on the combined SSMIS and ASCAT observations to identify spatio-temporal patterns of satellite observations. These patterns are then compared with the ~~ρ_{12cm}~~ density patterns obtained from IMAU-FDM, and dry-snow zones are determined (Sect. 3.2). Finally, we quantify the potential of a non-linear Random Forest (RF) machine learning approach trained on SSMIS and ASCAT observations to derive the spatial and temporal variations in dry firn density (Sect. 3.3). For clarity, the content of Sect. 3.2 and Sect. 3.3 are summarised and visualised as a flowchart in Fig. 1.

3.1 Calculation of correlation between satellite parameters and firn density

To gain a general understanding of the spatial patterns of the satellite parameters and densities from IMAU-FDM, we calculate and visualise the map of T_B ~~, σ^0, $PR(f)$, $FR(p)$ and the 12 cm firn density (ρ_{12cm})~~ and σ^0_A and the IMAU-FDM firn density at a selected depth averaged between Jan. 1 2011 and Dec. 31 2020 (shown in Appendix A). Then, to observe the temporal correlation between the satellite parameters and the IMAU-FDM densities, for each pixel, the correlation coefficient between different satellite parameters and the firn density over time is calculated and visualised. To ensure consistent temporal resolution for the analysis, the satellite parameters are downsampled from daily resolution to 10-day resolution to match the temporal resolution of the IMAU-FDM densities. Since the scattering properties of microwave are affected by firn properties along the penetration depth (Ulaby et al., 1996; Bingham and Drinkwater, 2000; Arndt and Haas, 2019; Cartwright et al., 2022), this analysis utilises densities from a range of depths, including 12 cm, 40 cm, 1 m, 2 m, 5 m and 10 m. The density of each depth is defined not as the specific density at the single depth, but the average density from the surface to this depth. Finally, the density at the depth where the best overall correlation between satellite observations and density time series is adopted for the RF experiment.

3.2 Characterisation of firn types using time series of microwave observations

In our study, the ~~spatial~~ clustering of satellite observations is primarily carried out as a preparatory step aiming at ensuring that all the representative regions, i.e. the regions with distinctive satellite data patterns, are correctly accounted for ~~into~~ in the RF model training procedure in Sect. 3.3. Moreover, we aim to rule out pixels where melt events can be observed, as

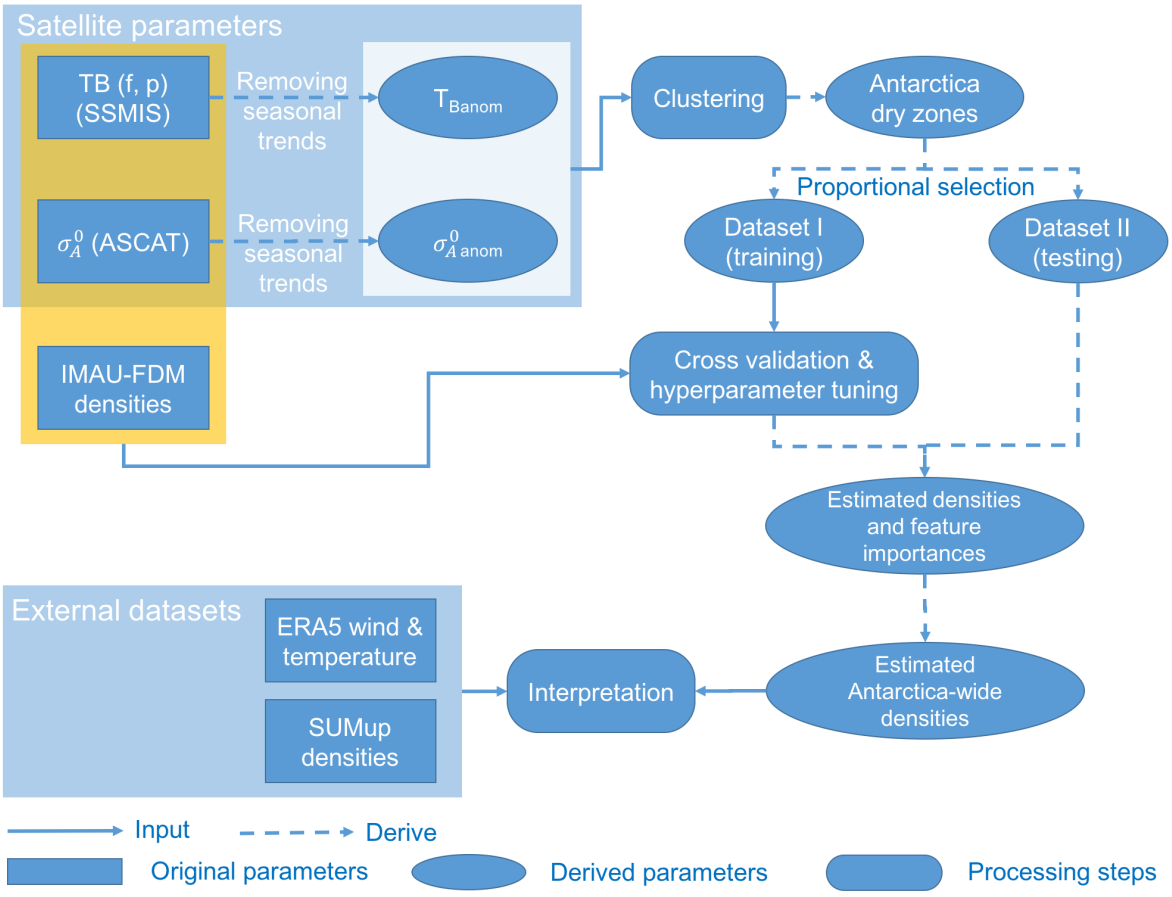

Figure 1. Overview flowchart of the data and method used in this study. The clustering process uses T_{Banom} and ~~σ^0_{anom}~~ σ^0_{Aanom} as input to derive dry snow zones over the Antarctic ice sheet. Then, pixels clustered as dry snow are included to estimate firn density with the RF regressor. Parameters used as features of the RF regressor are further elaborated in Sect. 3.3. ~~Blocks coloured in orange represent the hyperparameters and the RF model that are not tuned.~~ Among the derived parameters, Antarctica dry zones, Dataset I and Dataset II are ~~collections~~ selected proportionally based on the number of pixels ~~, therefore the parameters within these pixels are indicated by orange arrows before being used as input to the RF regressors~~per cluster.

the melt-induced liquid water and ice-lens formation complicates the satellite measurements (Stiles and Ulaby, 1980; Brucker et al., 2010; Trusel et al., 2012), rendering density estimations invalid in such cases. ~~By performing spatial clustering, we aim to capture the diversity of satellite data patterns and incorporate them into the subsequent analysis.~~ This step facilitates a comprehensive understanding of the spatio-temporal variations of firn properties based on the available satellite observations. We expect that clustering the time series of satellite observations will effectively differentiate pixels experiencing melting from those unaffected. By identifying and excluding melt-affected pixels, we can ensure the validity of density estimations using the RF regressor described in Sect. 3.3. Additionally, to enhance the ability of the RF regressor to capture the characteristics of various dry snow types, we choose training samples based on the identified dry snow types. This approach enables the representation of diverse snow types in the training dataset, improving the accuracy of the RF regressor in estimating density across different snow types.

To cluster and distinguish the different snow types, we propose to use the anomalies in T_B and ~~σ^0~~ σ^0_A described as follows. Since T_B is strongly dependent on seasonal variations of firn temperature, the average seasonal signal is removed in the clustering process to obtain time series anomalies that reflect the variations of temporary events such as melt–refreeze (Nicolas et al., 2017) and density or grain size variations (Picard et al., 2012; Champollion et al., 2013). We also derive the ~~σ^0~~ σ^0_A anomalies due to the impact from temperature seasonal cycles (Fraser et al., 2016). The time series anomalies are calculated by taking the ten-year average of T_B or ~~σ^0~~ σ^0_A for each day in a year, defined as $\overline{T}_B$ and ~~$\overline{\sigma}^0$~~ $\overline{\sigma}^0_A$, and subtracting this averaged time series from the absolute observations for each year, leading to $T_{Banom} = T_B - \overline{T}_B$ and ~~$\sigma^0_{anom} = \sigma^0 - \overline{\sigma}^0$~~ $\sigma^0_{Aanom} = \sigma^0_A - \overline{\sigma}^0_A$. The time series anomalies of T_{Banom} and ~~σ^0_{anom}~~ σ^0_{Aanom} are then normalised and stacked for clustering.

The adopted clustering solution is a simple hierarchical algorithm (Ward, 1963) which uses the normalised and stacked T_{Banom} and ~~σ^0_{anom}~~ σ^0_{Aanom} time series as input. For pre-processing, we remove outliers in the T_{Banom} and ~~σ^0_{anom}~~ σ^0_{Aanom} time series per pixel by defining an interval of three standard deviations above and below average. Then, the temporal gaps are filled with a linear interpolation. The application of the clustering algorithm is illustrated with an example (Fig. 2). The clustering process starts from all clusters each containing one pixel, and the clusters are then hierarchically grouped together based on the similarity of features, which refers to the euclidean distance between the normalised and stacked T_{Banom} and ~~σ^0_{anom}~~ σ^0_{Aanom} time series of different pixels in our study (however only ~~σ^0_{anom}~~ σ^0_{Aanom} from January 14, 2016 is used in Fig. 2 for illustration). The grouping process is typically represented by a dendrogram, as in Fig. 2b. Finally, the number of clusters is determined empirically; different numbers of clusters result in different outcomes, as in Fig. 2c–e. For our study where the normalised and stacked T_{Banom} and ~~σ^0_{anom}~~ σ^0_{Aanom} time series between 2011 and 2020 are used, we select 7 clusters as the optimal number of clusters. ~~Following the clustering process~~To provide a brief overview of the clustering result, we visualise the time series of the mean, 20th percentile, and 80th percentile of different satellite parameters, together with ~~the~~ an IMAU-FDM ~~ρ_{12cm}~~ density for each cluster in Appendix B. This allows a comparison of the changes in satellite parameters with density variations across the clusters and an assessment of the reliability of our study to distinguish melt zones from dry ones.

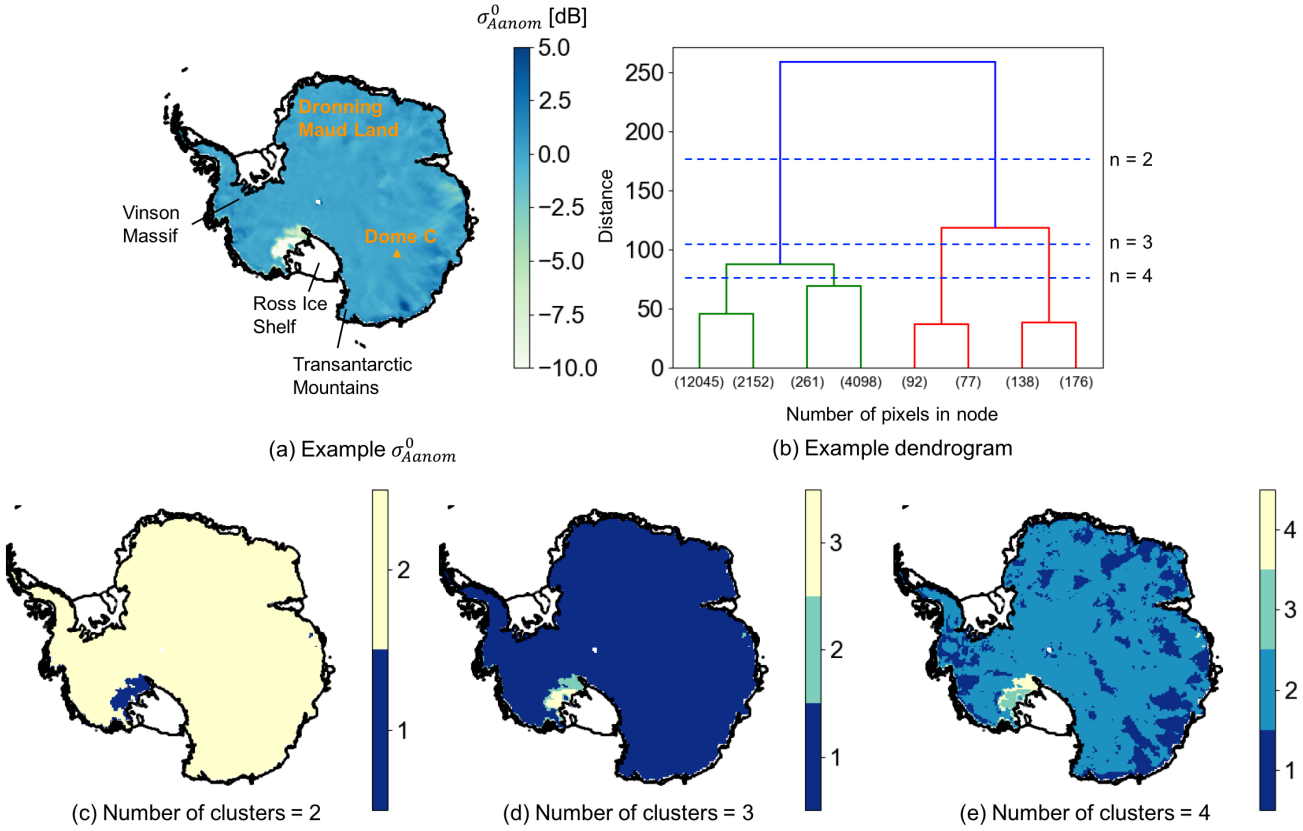

Figure 2. An example of the principle of hierarchical clustering. (a) Map of ~~σ^0_{anom}~~ σ^0_{Aanom} acquired on January 14, 2016 following the melt event detected by Nicolas et al. (2017), (b) dendrogram obtained from (a), with low-hierarchy nodes simplified and n referring to number of clusters, and (c)–(e) clustering results using different numbers of clusters. ~~Dome C is~~ Several locations mentioned in this study are labelled in (a)~~as a major location of interest in this study~~. The coastline is from Depoorter et al. (2013).

3.3 Deriving firn densities using satellite parameters and random forest regressor

Given the complex and often non-linear relationships between satellite observations and firn density (Fraser et al., 2016), a non-linear regression model based on machine learning is explored to relate the satellite time series to firn density. The method relies on a certain amount of known density measurements as the training dataset, and on the continuous satellite parameters as the trained features. We opt for a random forest regressor as machine learning model (RF regressor hereafter) due to the simplicity and usability (Vafakhah et al., 2022; Viallon-Galinier et al., 2023).

Ideally, in situ measurements should be used as the training dataset. However, in situ measurements are often single measurements that lack temporally continuous observations. As our goal is to relate the satellite time series to assess spatio-temporal variations in firn density, we adopt an alternative approach that uses the output of IMAU-FDM as training data instead of rely-

ing on in situ data. Although this approach has the disadvantage of training the RF regressor on a noisy IMAU-FDM dataset, which may exhibit spatial and temporal differences compared to actual in situ densities (e.g., biases between the model and in situ observations), we leverage the strengths of RF regression for pattern recognition in noisy datasets. The use of multiple decision trees and random feature selection can reduce the variance of the model and reduce overfitting, resulting in better generalisation performance on noisy data (Hastie et al., 2008). Therefore, we expect that the RF regressor generalises on the density estimations of IMAU-FDM, which is known to capture the spatial variation of in situ density measurements well and the temporal variations reasonably well (Veldhuijsen et al., 2023).

The training, testing, and implementation of the RF regressor involve three main steps:

- Training and Hyperparameter Tuning: a subset of IMAU-FDM densities (Subset I) is used as the training dataset in a 5-fold cross-validation procedure. Multiple models are evaluated, representing different combinations of hyperparameters defined for the RF regressor (see Table 1). The goal is to identify the configuration that achieves the best cross-validation score, indicating the optimal set of hyperparameters for the RF regressor.

- Testing and Model Evaluation: a different subset of temporally and spatially coregistered SSMIS and ASCAT measurements for the given pixels (Subset II) is used as input to the RF regressor, which has been trained on Subset I. The purpose of this step is to evaluate the performance of the model and assess the accuracy of the RF density estimations. Additionally, it helps to determine the importance of satellite parameters in the predictions of the regressor.

- Antarctica-wide Implementation: The satellite time series covering the entire study area are fed into the RF regressor, which has been trained on Subset I. This step aims to estimate densities across the entire Antarctic dry-firn region. The output densities are then evaluated by comparing them to both the IMAU-FDM densities and the SUMup densities.

Both Subset I and Subset II consists of pixels randomly selected from the non-melting pixels clustered in Section 3.2. Subset I contains 10 % of the non-melting pixels, and Subset II contains 100 pixels in total. The pixels from both subsets should not overlap. The time series of each feature in each pixel cover the period between January 1 2011, and December 31 2020 with a 10-day resolution. To ensure consistent temporal resolution between the input features and the target IMAU-FDM densities, the daily satellite parameters are also downsampled to the 10-day temporal resolution of the IMAU-FDM firn density by selecting the corresponding acquisition date, resulting in 366 samples in total for each feature in each pixel. Finally, Subset I consists of 1,748 pixels multiplied by 366 samples (639,768 samples in total), Subset II consists of 100 pixels multiplied by 366 samples (36,600 samples in total), and the Antarctica-wide dataset consists of 17,478 pixels multiplied by 366 samples (6,396,948 samples in total).

The RF regressor is implemented with the target variable $\rho_{\mathrm{T2}cm}$, which is the IMAU-FDM density at the depth selected from the correlation analysis, and input features $\boldsymbol{X}$ initially defined as follows:

$$\boldsymbol{X} = (T_B(19V),\ T_B(19H),\ T_B(37V),\ T_B(37H),\ \sigma^0_A) \tag{2}$$

Table 1. Hyperparameter range and optimal values used to specify the random forest (RF) model.

Hyperparameter	~~Hyperparameter range~~ Range	Optimal ~~hyperparameter~~ value
Number of trees	~~200, 300, 400~~ 50, 100, 200	~~400~~ 100
Maximum depth of the tree	12, 15, 18	~~18~~ 12
The minimum number of samples at a leaf node	1, 3, 5, 7	~~1~~ 5
~~The number of features to consider when searching for the best split 1, 3, 5, 7 3 The~~ The minimum number of samples to split an internal node	2, 3, 4, 5	4
The number of features to consider when searching for the best split	1, 3, 5	~~3~~ 1

Within $\boldsymbol{X}$, we include T_B and ~~σ^0~~ σ^0_A to account for variations in temperature, precipitation and other potential climate parameters that show a potential strong seasonality (e.g., Fraser et al., 2016)~~, whereas the anomalies in T_B, σ^0, $PR(f)$ and $FR(p)$ are included to account for temporal and spatial variations relative to the seasonal cycle. Moreover, we exclude melting pixels from the RF regressor as melt potentially disturbs the satellite parameters. However, the setting of $\boldsymbol{X}$ may be arguable, as (i) $PR(f)$ and $FR(p)$ are computed based on multiple T_B channels, therefore may not bring additional information independent of the original T_B time series, and (ii) T_{Banom} and σ^0_{anom} may not provide clear physical explanation in dry snow zones, therefore may not be informative in the estimation of densities. Given these concerns, we consider the following settings $\boldsymbol{X_1}$ and $\boldsymbol{X_2}$:~~

$$\boldsymbol{X_1} = (T_B(19V),\ T_B(19H),\ T_B(37V),\ T_B(37H),\ \sigma^0$$

~~and~~

$$\boldsymbol{X_2} = (T_B(19V),\ T_B(19H),\ T_B(37V),\ T_B(37H),\ \sigma^0,\ PR(19GHz),\ PR(37GHz),\ FR(V),\ FR(H))$$

~~for a sensitivity analysis. However, hyperparameters of different settings should be tuned accordingly. We present the analysis in Appendix B.~~ .

In the testing and evaluation step, we assess the performance of the optimal RF regressor. This is achieved by comparing the RF and IMAU-FDM densities of Subset II using ~~scatterplots~~ a scatterplot and standard evaluation metrics, i.e. the root mean square error (RMSE) and the correlation coefficient between the RF densities and the IMAU-FDM densities. The importance of satellite parameters in the RF regressor is computed by calculating the Gini importance and the permutation importance. Gini importance in RF regression is a measure of feature importance based on the Gini gain, i.e. impurity reduction (Strobl

et al., 2007). For each feature used to split the data, the decrease in the Gini node impurity is recorded at each split, and the Gini importance is calculated as the average of all decreases in the Gini impurity in the forest where this feature forms the split (Archer and Kimes, 2008). ~~The permutation importance uses the out-of-bag (oob) observations for each tree, which are observations in the data that are not used to form the tree. The values of each feature in the oob data are randomly permuted, and the permutation importance is calculated as the average decrease in accuracy between the oob observations and permuted oob observations (Breiman, 2001; Archer and Kimes, 2008). The Gini importance can be biased as it depends on statistics of the training dataset (Sandri and Zuccolotto, 2009), however it is an indicative information from the RF regressor.~~

~~Finally, in~~ In the Antarctic-wide implementation, the optimal RF regressor is implemented to predict the spatial and temporal variations in firn density. These predictions are then compared with IMAU-FDM and the SUMup densities. The spatial agreement is assessed by comparing the temporal averages of the RF predictions, IMAU-FDM and SUMup by using the mean difference and the RMSEs. The temporal agreement is assessed by the RMSE and the correlation coefficient between the per-pixel time series of RF predictions and IMAU-FDM ~~predictions and the correlation coefficient~~density. We also compare the spatial patterns of the RF-predicted densities with the ERA5 ~~climate parameters of surface temperature and~~ wind velocity as ~~these are potential drivers~~ it is a potential driver for spatial variation in firn density, especially for the uncertainties of IMAU-FDM. Finally, we illustrate this temporal agreement by showing time series over ~~eight random pixels and Dome C (E~~ four pixels that show representative differences between RF and IMAU-FDM densities (locations visualised in Fig. 4)~~, where extensive studies have been performed (Champollion et al., 2013; Brucker et al., 2014; Leduc-Leballeur et al., 2017).~~ .

In addition, since satellite parameters may exhibit a certain level of correlation with densities in the long term (Fraser et al., 2016) , we also conduct a linear regression (LR) process, which fits a linear function between $\boldsymbol{X}$ and the target density. The RMSE and correlation coefficient between the LR-obtained density and IMAU-FDM density are also used to assess the advantages and drawbacks of RF.

4 Results

4.1 Correlation between satellite parameters and firn density

The temporal correlation between satellite parameters and the average density from the upper x m depth (x refers to 12 cm, 40 cm, 1 m, 2 m, 5 m and 10 m, respectively) is calculated per pixel, and the spatial average of the correlation coefficient is summarised in Table 2. The results show that on average, the maximum absolute correlation coefficient can be obtained at 40 cm depth. The correlation between density and T_B at 19 GHz frequency drastically decreases at 5 m, and between density and T_B at 37 GHz frequency largely decreases at 2 m, similar to the penetration ability from Surdyk (2002). The correlation between densities and σ^0_A is constantly negative, and the absolute correlation coefficient is constantly low; however, it also demonstrates a slight decrease as the depth increases from 2 m to 10 m, showing a certain degree of sensitivity. Despite the low correlation, however, our study still includes σ^0_A due to the long-term correlation derived by Fraser et al. (2016).

The lack of spatial and temporal consistency between satellite and density is illustrated in Fig. 3, which shows the pixel-wise temporal correlation of each satellite parameter with the ~~12~~40 cm density in IMAU-FDM. All T_B channels generally show a

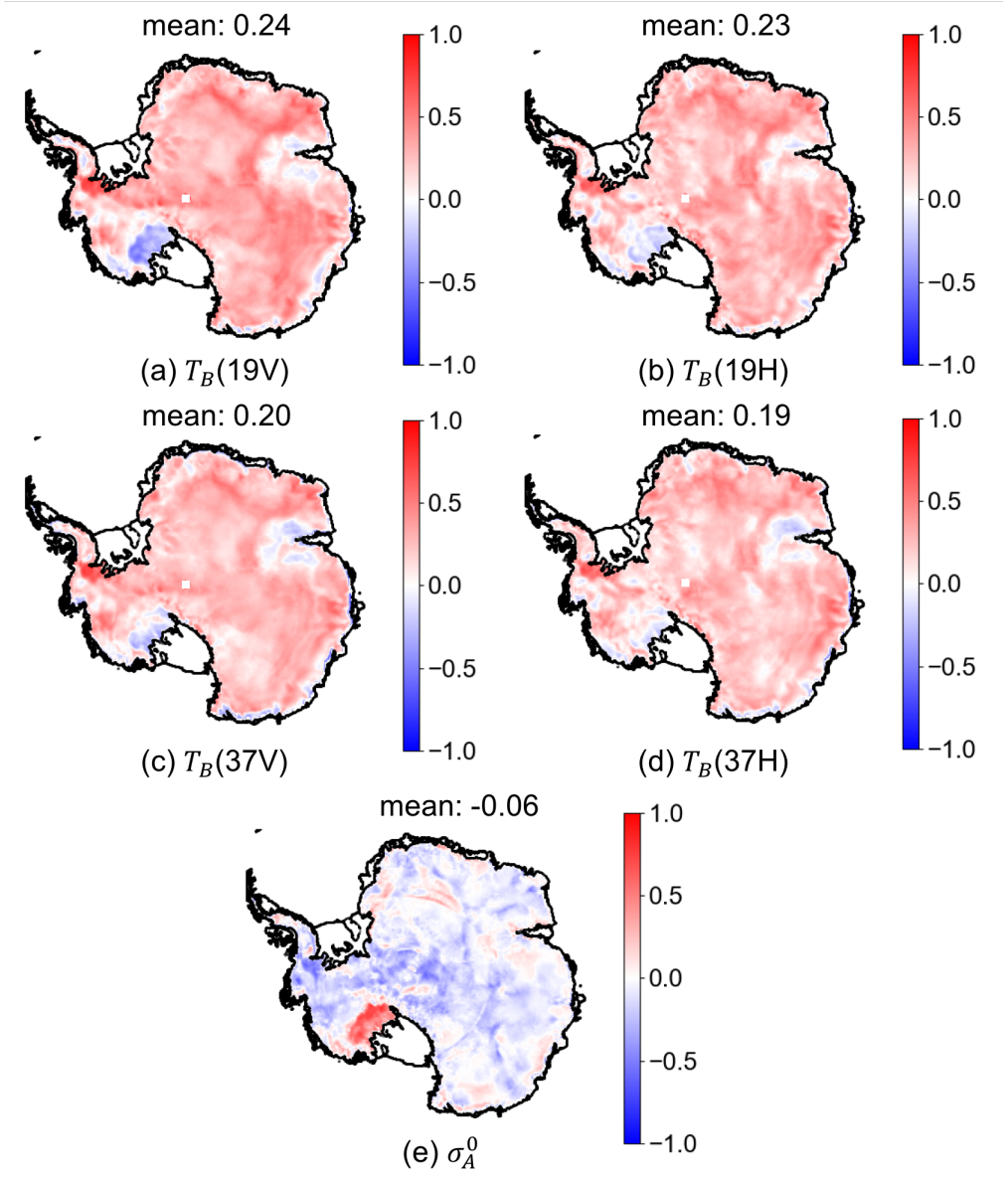

Figure 3. Map of temporal correlation calculated per pixel between ~~12~~40 cm IMAU-FDM density and (a) brightness temperature (T_B) from 19 GHz vertical polarisation, (b) T_B from 19 GHz horizontal polarisation, (c) ~~polarisation ratio from 19 GHz ($PR(19GHz)$), (d)~~ T_B from 37 GHz vertical polarisation, (~~e~~d) T_B from 37 GHz horizontal polarisation, ~~(f) polarisation ratio from 37 GHz ($PR(37GHz)$), (g) frequency ratio from vertical polarisation ($FR(V)$), (h) frequency ratio from vertical polarisation ($FR(H)$),~~ and (~~i~~e) backscatter intensity ($~~\sigma^0~~\sigma^0_A$). The coastline is from Depoorter et al. (2013).

Table 2. Average temporal correlation coefficient between satellite parameters and IMAU-FDM density from different depths.

Depth	$T_B(19V)$	$T_B(19H)$	$T_B(37V)$	$T_B(37H)$	σ^0_A
12 cm	0.19	0.18	0.20	0.20	-0.05
40 cm	0.24	0.23	0.20	0.19	-0.06
1 m	0.23	0.20	0.12	0.12	-0.06
2 m	0.18	0.12	0.03	0.02	-0.06
5 m	0.08	0.02	-0.07	-0.08	-0.04
10 m	0.05	0.01	-0.07	-0.07	-0.03

positive correlation with ~~ρ_{12cm}~~ ρ_{40cm} in East Antarctica, but a negative correlation in parts of West Antarctica and many coastal regions. The negative correlation in coastal regions can be attributed to melt, as shown in the masked out regions in Fig. 4 of Picard et al. (2012). ~~Vertical polarisation T_B shows higher correlations compared to horizontal polarisation, and 19 GHz T_B shows higher correlations than 37 GHz T_B. Contrary to the findings of Champollion et al. (2013), $PR(f)$ does not show a consistently positive correlation with ρ_{12cm}, especially at the location of Dome C, where the correlation coefficient between ρ_{12cm} and $PR(19GHz)$ is -0.21, and between ρ_{12cm} and $PR(37GHz)$ is -0.30. Most pixels show a negative correlation between ρ_{12cm} and $FR(p)$, except for coastal regions that show positive correlation. Finally, the correlation between ρ_{12cm} and~~ The correlation between ρ_{40cm} and σ^0 is generally low, except for the region next to the Ross Ice Shelf (location shown in Fig. 2a, where the correlation coefficient ~~is up to 0.5~~can be up to 0.75.

Overall, this correlation analysis indicates that the relationship between satellite parameters and firn density is complex, and simple linear relationships ~~cannot~~ may not adequately describe the IMAU-FDM density based on different satellite parameters. Therefore, non-linear approaches such as the RF regressor should be employed to assess the potential of relating the IMAU-FDM firn density to various satellite parameters (Vafakhah et al., 2022; Anilkumar et al., 2023).

4.2 Firn-type clusters

Figure 4 shows the map of clusters derived from time series of the combined satellite parameters, where each cluster represents a natural grouping of pixels with similar satellite time series behaviour. The map shows that four large clusters (referred to as Firn 1–4) cover the dry firn interior of Antarctica. Firn 1–3 in East-Antarctica and Firn 4 in West-Antarctica. Firn 5 is a cluster in West Antarctica close to Ross Sea which corresponds to the region that showed a strong melt event in Jan. 2016 (Nicolas et al., 2017) while Firn 6 and Firn 7 show small regions near the coastline in East- and West-Antarctica respectively that also show clear melting signals ~~.~~ (details shown in Appendix B).

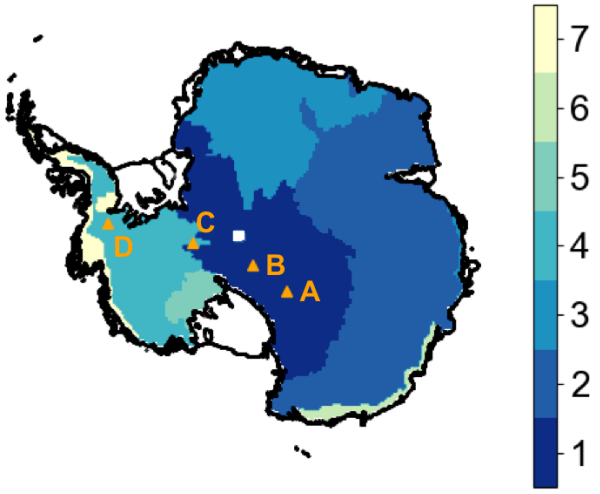

Figure 4. Clustering results from the combination of normalised T_B and ~~σ^0~~ σ^0_A after removing the seasonal trend. Triangles show the locations where temporal assessment per pixel is performed. The coastline is from Depoorter et al. (2013).

~~Time series of mean (curves) and 20th–80th percentiles (shaded areas) of the clustering results in Fig. 4, (a)–(g) corresponding to Snow facies 1–7. The visualised satellite observations are: time series anomalies of brightness temperature (T_B) from 19 GHz and 37 GHz, both horizontal and vertical polarisation ($T_{B_{anom}}(19V)$, $T_{B_{anom}}(19H)$, $T_{B_{anom}}(37V)$ and $T_{B_{anom}}(37H)$, respectively), polarisation ratio from 19 GHz ($PR(19GHz)$) and 37 GHz ($PR(37GHz)$), frequency ratio from vertical polarisation ($FR(V)$) and horizontal polarisation ($FR(H)$), time series anomalies of backscatter intensity (σ^0_{anom}), and IMAU-FDM density at 12 cm (ρ_{12cm}) depth. The colours of the curves correspond to the legends in (g).~~

~~Figure B1 presents the time series of the mean and 20th–80th percentiles of each parameter for each cluster, (a)–(g) corresponding to clusters 1–7, respectively. Clusters Firn 1–4 exhibit small and short-term variations in T_{Banom} and $\sigma^0 anom$; the extent of variations differ between different clusters. Firn 1 has the smallest variations in T_{Banom} and σ^0_{anom}, which are within ±5 K and ±0.25 dB, respectively. Firn 2 and Firn 3 have a T_{Banom} between −5 K and 10 K, however, Firn 2 has a σ^0_{anom} within ±1 dB, while Firn 3 has a σ^0_{anom} within ±0.5 dB. Firn 4 is characterised by a T_{Banom} variation within ±10 K and a σ^0_{anom} variation within ±0.5 dB. Finally, the $PR(f)$ and $FR(p)$ time series of Firn 1–4 undergo regular and similar seasonal cycles.~~

~~On the contrary, clusters Firn 5–7 all show large and abrupt variations in T_{Banom} and σ^0_{anom}, mainly as a result of melt events (e.g., Nicolas et al., 2017) that drastically change absorption, emission and scattering of microwave radiation and thus the T_{Banom} and σ^0_{anom}. The effects of these melt events are also evident in the time series of $PR(f)$, $FR(p)$, and the IMAU-FDM densities, as the abrupt changes in firn density are associated with the occurrence of melt events (Amory et al., 2024). For example, this can be clearly seen in the time series of cluster Firn 5, where the melt event of 2016 shows a prolonged effect on the σ^0_{anom} time series due to the formation of a sub-surface refrozen high-density layer in IMAU-FDM. The high-density layer~~

~~is detected by the scatterometer with stronger snow penetrating capability. In IMAU-FDM, this high density layer appears also in ρ_{12cm} where it increases by approximately 100 $kg\ m^{-3}$. The comparison of all clusters highlights the dominant influence of melt events on T_{Banom} and σ^0_{anom} in the wet-firn pixels, whereas the dry-firn pixels exhibit a more pronounced seasonal variation in satellite parameters. It is important to note that the wet firn clusters are not used in the following RF steps due to the complex impact of the melt–refreeze cycle on satellite observations.~~

4.3 Assessment of RF densities at sample pixels

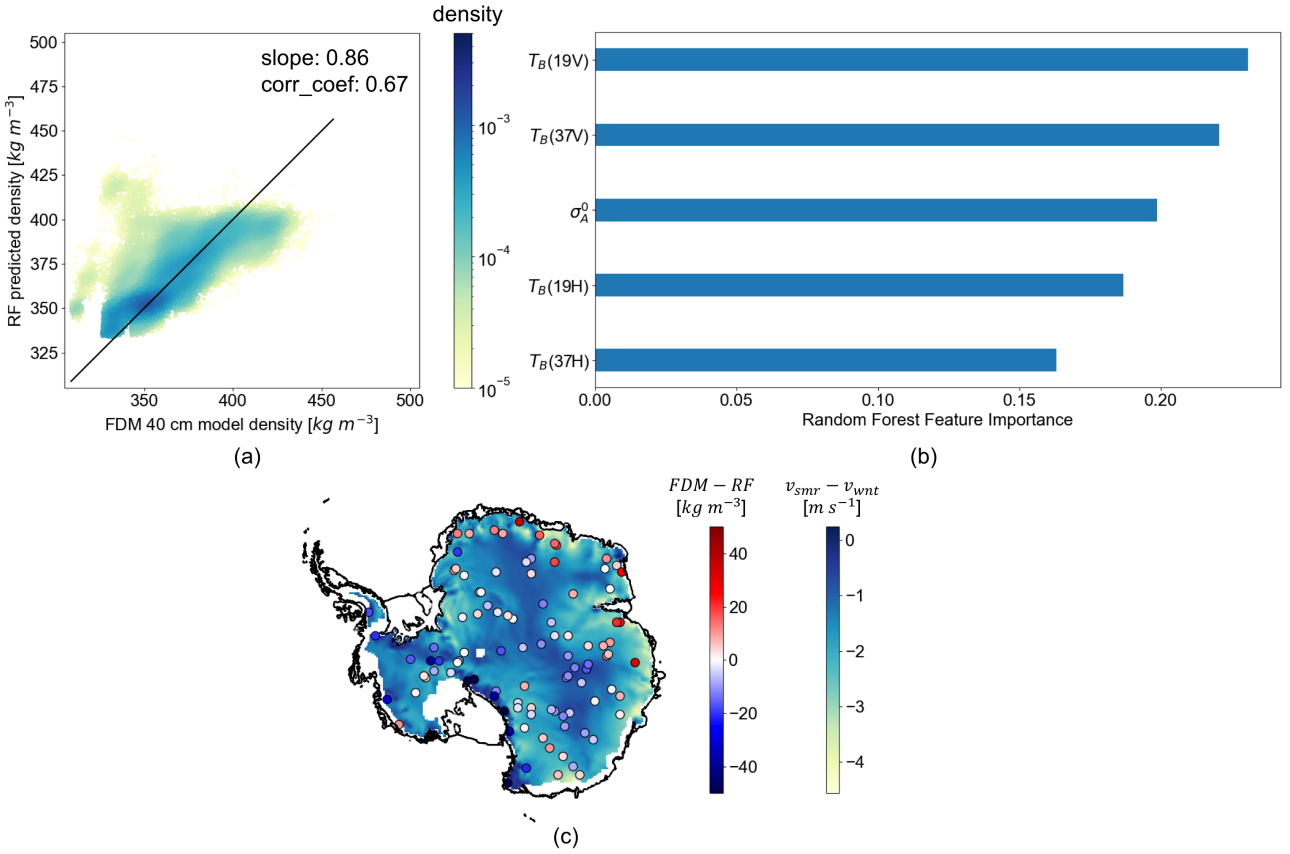

Figure 5. (a) Density comparison between RF densities and IMAU-FDM densities at sample pixels referred to as Subset II, the colour of the points showing the ~~spatial~~ density distribution of points~~nearby~~; the colour bar is in logarithmic scale, (b) RF feature importance of different input satellite parameters, and (c) ~~permutation importance~~ the temporally averaged difference between IMAU-FDM and RF densities at the pixels, visualised on top of ~~different input satellite parameters~~the map of the difference between the summer (v_{smr}) and winter wind velocity (v_{wnt}) from ERA5. The coastline is from Depoorter et al. (2013).

Figure 5a presents the results of the RF regressor for estimating firn densities based on satellite parameters. It demonstrates that the non-linear multivariate approach of the RF regressor captures the spatial variations in IMAU-FDM density, exhibiting a

linear relationship between IMAU-FDM and RF densities with a slope of ~~1.000~~0.86. The RMSE is ~~16.57 $kg\ m^{-3}$~~ 19.23 $kg\ m^{-3}$ and the correlation coefficient between the estimated and training densities is ~~0.780~~0.67. Moreover, the RF regressor performs most ideally between approximately 325 $kg\ m^{-3}$ and 375 $kg\ m^{-3}$, whereas it fails to capture the large densities as no RF estimate exceeds ~~450 $kg\ m^{-3}$~~410 $kg\ m^{-3}$, which can partially be due to a well-known extrapolation problem intrinsic to the RF regression (Hengl et al., 2018). The RF densities also exhibit an overestimation when the IMAU-FDM density is lower than 325 $kg\ m^{-3}$. The pixels with large overall underestimation (in dark red) and overestimation (in dark blue) of RF is also visible in Fig. 5c. In general, the large underestimation of RF occurs in the coastal regions of East Antarctica, where the winter wind velocity largely exceeds the summer wind velocity (by approximately 3 $m\ s^{-1}$). The large overestimation of RF occurs along the Transantarctic Mountains, where the topography is more complex, introducing strong surface scattering instead of volume scattering. The feature importance provided by Gini impurity index (Fig. 5b) shows the ranked importance of satellite parameters in the predictive performance of the model, indicating that the ~~raw~~ vertical polarisation of T_B ~~and σ^0 observations are more important than the PR and FR ratios and the anomalies in predicting the ρ_{12cm}. The dominance of T_B is understandable as both T_B and ρ_{12cm} are dependent on firn temperature. This correlation is~~ is dominant in predicting ρ_{40cm}. The higher importance of 19 GHz is also clearly visible in the temporal correlation coefficients in Fig. 3. We attribute the high importance of σ^0 to the fact that it can be influenced by other parameters that have an impact on dry-snow scattering properties, such as wind and precipitation; the mechanism may not necessarily be linear, but rather complex (Fraser et al., 2016). ~~Among the derived satellite observations ($PR(f)$ and $FR(p)$), $FR(V)$ has the highest importance. The T_B time series anomalies overall show little importance, which can also be observed in Fig. B1, where the T_B time series anomalies are mainly high-frequency signals that do not correspond to changes in densities in dry-firn regions. The permutation importance in Fig. 5c, demonstrates different rankings of importance from the RF importance in T_B, σ^0 and T_B ratios. However, the low importance of time series anomalies remains.~~

4.4 Spatial assessment of RF densities

In Fig 6, the temporally averaged RF density estimates and their differences relative to IMAU-FDM densities at the ~~12 cm~~ 40 cm depth and SUMup in situ densities are presented. The comparison in Fig. 6c shows that temporally averaged RF density estimations are in general larger than temporally averaged IMAU-FDM density in interior regions of Antarctica except for megadune regions, whereas they are lower towards coastal regions. The RMSE between the IMAU-FDM and RF averages (referred to as FDM-RF) is ~~13.38 $kg\ m^{-3}$~~ 17.30 $kg\ m^{-3}$ and the mean FDM-RF difference is $-0.40\ kg\ m^{-3}$. An overestimation of RF is most pronounced in West Antarctica close to Vinson Massif (location shown in Fig. 2a), which possibly corresponds to the overestimation in Fig. 5a. Meanwhile, the comparison with the SUMup densities shows that RF and IMAU-FDM densities have comparable error patterns. The RMSE of FDM-SUMup is ~~58.03 $kg\ m^{-3}$~~59.17 $kg\ m^{-3}$, and the mean of FDM-SUMup bias is ~~20.68 $kg\ m^{-3}$~~23.92 $kg\ m^{-3}$; the RMSE of RF-SUMup is ~~60.36 $kg\ m^{-3}$~~62.22 $kg\ m^{-3}$, and the mean of RF-SUMup is ~~22.10 $kg\ m^{-3}$~~26.46 $kg\ m^{-3}$. This shows a general overestimation and a large bias of both IMAU-FDM and the RF models when validated with the SUMup measurements. In Fig. 6d, it can be observed that neither IMAU-FDM nor RF manages to follow the large SUMup dynamics. This difference between models and in situ measurements can be attributed to the temporal

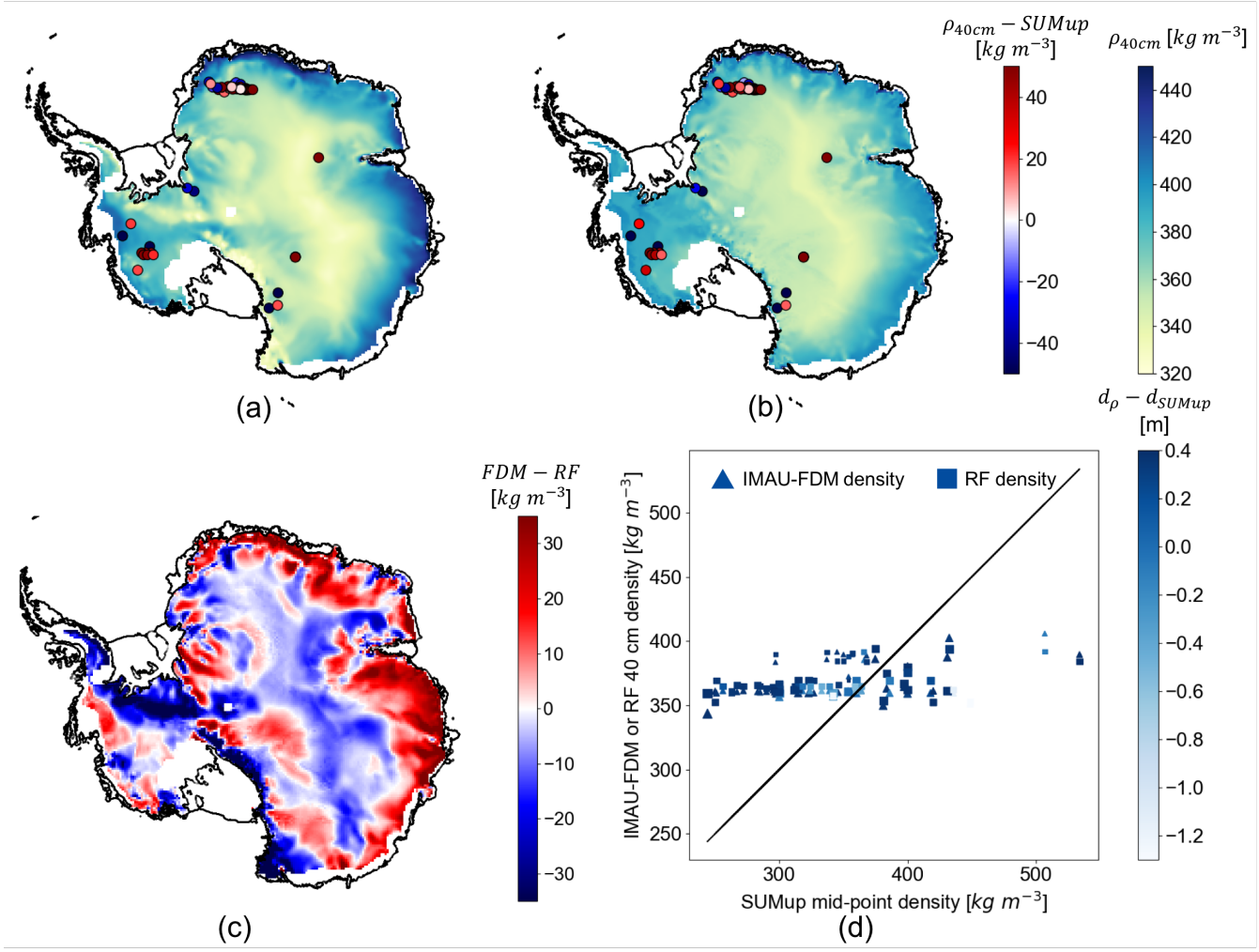

Figure 6. (a)–(c) Maps of (a) temporally averaged IMAU-FDM ~~12~~40 cm densities, (b) temporally averaged RF densities, (c) difference between averaged IMAU-FDM densities and RF densities ($FDM - RF$). Difference between the modelled or estimated densities and the SUMup densities are shown in scattered points in (a) and (b) as FDM-SUMup or RF-SUMup. (a) and (b) share the same colour bar, in which blue–red shows the difference between the IMAU-FDM or RF densities and the SUMup densities (~~$\rho_{12cm} - SUMup$~~$\rho_{40cm} - SUMup$), and green–light blue shows the IMAU-FDM or RF densities (~~ρ_{12cm}~~ρ_{40cm}). The coastline is from Depoorter et al. (2013). (d) shows the relationship between IMAU-FDM or RF densities and SUMup densities. The sizes of the scattered points indicate the time difference between the SUMup measurements and year 2020, and the colour shows the difference in depth between IMAU-FDM or RF measurements (both fixed at ~~12~~40 cm) and SUMup measurements ($d_\rho - d_{SUMup}$).

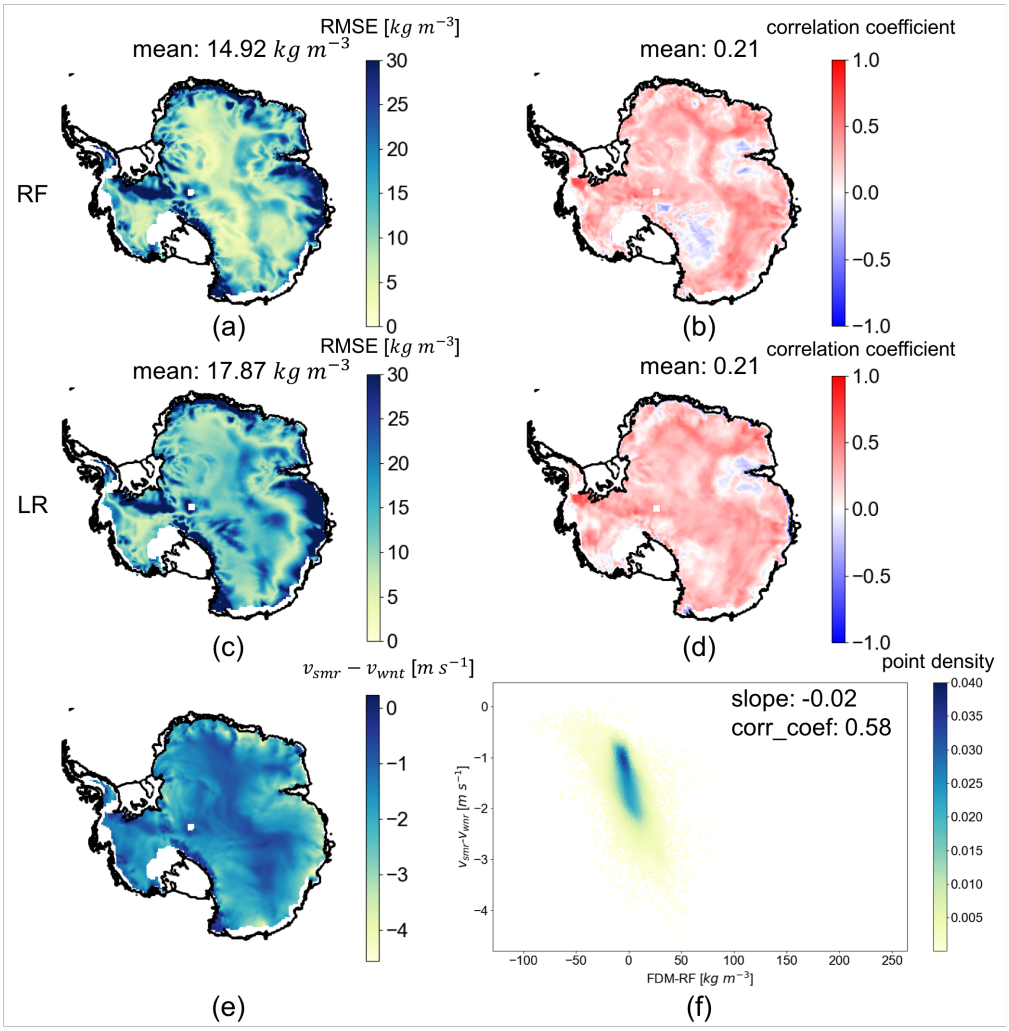

Figure 7. Map of (a) root mean square error (RMSE) between IMAU-FDM ~~12~~40 cm densities and RF densities, (b) the correlation coefficient between IMAU-FDM ~~12~~40 cm densities and RF densities, (c) ~~the difference between the summer~~ root mean square error (~~T_{smr}~~RMSE) between IMAU-FDM 40 cm densities and ~~winter temperature~~ LR densities, (~~T_{wnt}~~d) the correlation coefficient between IMAU-FDM 40 cm densities and LR densities, (~~d~~e) the difference between the summer (v_{smr}) and winter wind velocity (v_{wnt}) from ERA5, and (f) scatterplot of density difference between IMAU-FDM and RF versus the difference between summer and winter wind velocities, coloured by the density distribution of points. The coastline of the maps is from Depoorter et al. (2013).

discrepancies between the measurements and the IMAU-FDM and satellite observations, and the IMAU-FDM model errors or uncertainties that can also be learned by the RF regressor.

Aided by ~~Figure~~Fig. 7, we then analyse the temporal distribution of the offsets between the IMAU-FDM densities and the RF densities in more depth. Figure 7a generally shows low RMSE between IMAU-FDM and RF densities in high-elevation regions of East Antarctica and part of West Antarctica. The errors increase towards the coastal regions. The low correlation coefficients in Fig. 7b indicate a low temporal agreement between IMAU-FDM and RF densities. Furthermore, the correlation coefficients are generally positive; high correlation coefficients (≥ 0.5) can mainly be observed in high-elevation regions of East Antarctica (except for megadune regions Fahnestock et al., 2000) and a part of West Antarctic Peninsula. The regions with high correlation coefficients also mainly correspond to regions with high correlation coefficients (≥ 0.5) in Fig. 3~~d, with the regions in West Antarctica close to Firn 5 (in Fig. 4)~~ a, with parts of West Antarctica as an exception, which generally matches the observation in Fig. 5 where ~~$T_B(37V)$~~ $T_B(19V)$ has the highest importance. The temporal mismatch and low correlation between IMAU-FDM and RF may be in part due to the modelling errors of IMAU-FDM. The density changes that are not modelled by the IMAU-FDM, but affect the satellite observations, are expected to degrade the quality of the RF regressor. The satellite data might be affected by other climate parameters that are not included in the IMAU-FDM model. The comparison with LR density shows that RF largely outperforms LR in terms of RMSE, especially in the interior of the ice sheet. While the average correlation coefficient is comparable between RF and LR, RF outperforms LR in high-elevation regions of East Antarctica, and performs worse in the megadune regions. By assessing the temporal agreement (mainly correlation coefficients) with ERA5 ~~parameters~~ wind velocity (Fig. 7~~c and d~~ d and e), we can learn that a high temporal correspondence is spatially correlated with ~~both a high surface temperature~~ a small wind velocity difference (>~~10 K~~ $-2.5\ m\ s^{-1}$) between Antarctic summer (Oct.–Mar.) and winter (Apr.–Sept.)~~, as well as a small wind velocity difference (>$-1.5\ m\ s^{-1}$) between Antarctic summer and winter~~. However, despite the small wind velocity difference and a relatively high temporal correspondence, the RMSE between IMAU-FDM and RF is high, in regions close to Vinson Massif and along Transantarctic Mountains (locations shown in Fig. 2a), indicating uncertainties potentially introduced by topography which has an impact on ~~course-resolution~~ coarse-resolution satellite data.

4.5 Temporal assessment of RF densities at random pixels

In Figure 8, individual pixels ~~from different clusters~~ are inspected to understand the temporal differences between IMAU-FDM and RF densities. Pixels ~~A–C are selected from cluster Firn 1, pixels D–F belong to Firn 2 (with E referring to Dome C), pixels G and H are from Firn 3, and pixel I is from Firn 4.~~ A shows a low RMSE as well as a low correlation. Pixel B shows a relatively low RMSE, but a negative correlation. Pixel C shows a reasonable correlation coefficient, but a large bias. Pixel D shows overall most ideal RF performance. From the time series, it is apparent that the RF density ~~estimates~~ estimations generally exhibit a stronger and more consistent seasonal cycle compared to the IMAU-FDM densities, which display a less consistent seasonal pattern with stronger inter-annual variations. This discrepancy explains the relatively low correlation coefficients, as only the pixels with similar seasonal cycles to the satellite observations (e.g., ~~panel I~~panels C and D) exhibit a higher correlation between the two datasets.

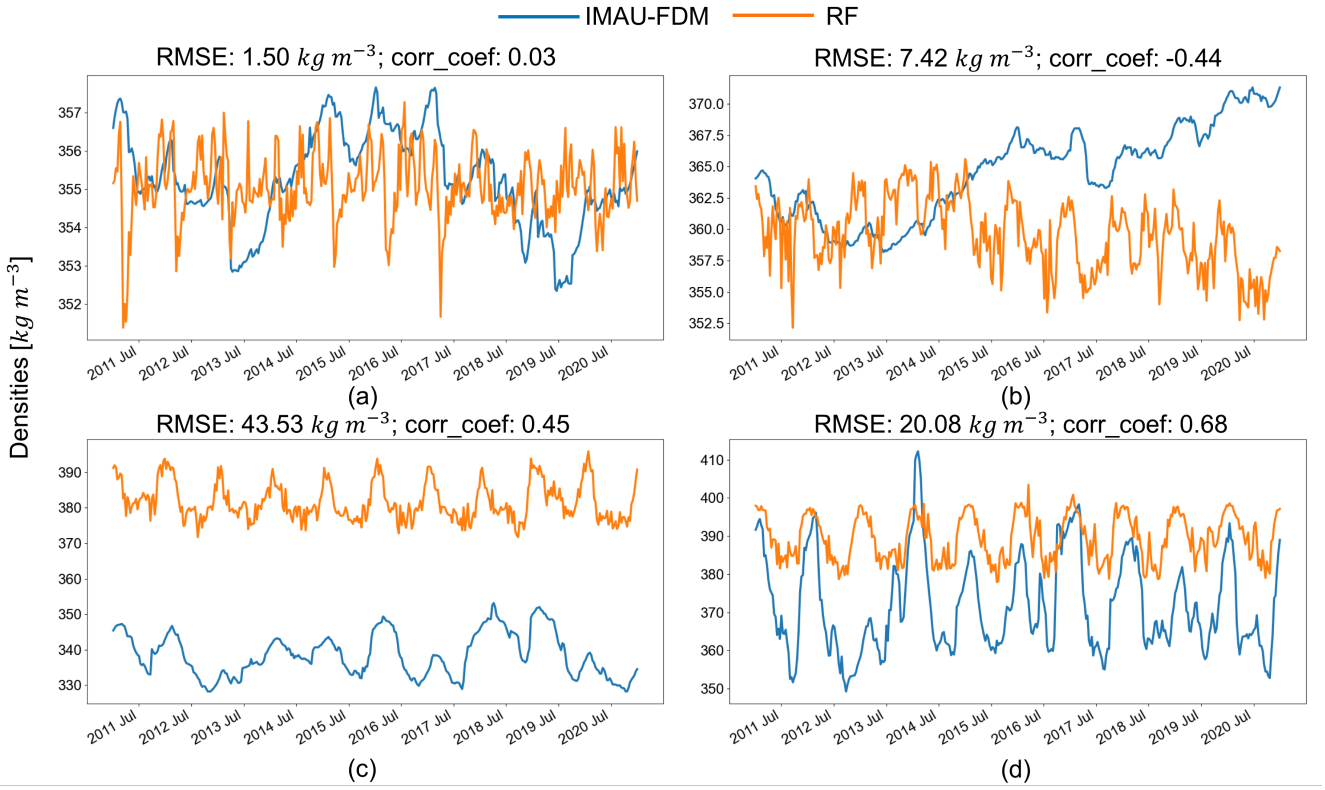

Figure 8. Comparison between time series of IMAU-FDM densities (in blue) and RF densities (in orange) at ~~8 randomly selected~~ 4 representative sample points and Dome C. Panels (a)–(~~i~~d) correspond to ~~A–I~~ A–D labelled in Fig.4. The RMSE and correlation coefficient (corr_coef) between the IMAU-FDM densities and the RF densities are shown above each figure.

~~In Figure ??, a comparison is made between the IMAU-FDM and in situ density measurements at Dome C (pixel E). The $PR(f)$ time series at both frequencies are also provided for comparison, as an increase in $PR(f)$ is theoretically correlated with the removal of the hoar layer, which is characterised by an increased density and a decrease in grain size. The comparison reveals that as the in situ densities vary between approximately 140 $kg\ m^{-3}$ and approximately 325 $kg\ m^{-3}$, the $PR(f)$ values from both frequencies quasi-concurrently vary by approximately 0.04. However, the concurrent 4 cm IMAU-FDM densities oscillate between 327 $kg\ m^{-3}$ and 329 $kg\ m^{-3}$, failing to capture the variation in the hoar layer observed in the in situ densities and the $PR(f)$ time series. This discrepancy between the IMAU-FDM densities and satellite observations also propagates to the 12 cm densities used in our study, and can undermine the importance of the $PR(f)$ time series in the RF estimation and subsequently affect the temporal performance of the RF regressor.~~

~~$PR(f)$ (in blue, left axis) with IMAU-FDM densities (in orange, middle axis) and densities from Leduc-Leballeur et al. (2021) (in yellow, right axis).~~

5 Discussion

In this study, we developed a novel approach to estimate Antarctic firn densities using satellite radiometer and scatterometer observations using a RF regressor and IMAU-FDM density outputs as reference data. Our ~~findings reveal~~ study is based on the complexity of the relationship between satellite ~~parameters~~ observations and firn density~~, as well as the limitations of linear models in capturing this relationship.~~.The lack of a consistent linear relationship was evident in ~~both the analysis of different satellite time series clusters and the~~ the examination of the individual satellite ~~parameters~~observations, as the highest mean temporal correlation between satellite observations and the 40 cm IMAU-FDM firn density is 0.24.

Our study first adopted an unsupervised machine learning method (hierarchical clustering) to distinguish dry snow zones from zones that experienced melt as a preparation step to the density estimation using the random forest (RF) regressor. In contrast to Tran et al. (2008), our study could distinguish melt occurrences, possibly based on the abrupt rise of T_B during melt (Johnson et al., 2020) and the ~~σ^0~~ σ^0_A rise due to ice-layer formation following melt events (Trusel et al., 2012). However, in some coastal regions in East Antarctica, our clustering method may be less sensitive to melt compared to Brucker et al. (2010) and Picard et al. (2012), resulting in more dry-snow pixels. Among dry-snow zones, Firn 1 consists of most interior regions, hence is characterised by the smallest variations in satellite parameters and is overall most stable, whilst Firn 4 is located in West Antarctica, hence is least stable with the largest variations in satellite parameters. The main difference between Firn 2 and Firn 3 is characterised by a larger ~~σ^0_{anom}~~ σ^0_{Aanom} variation in Firn 2; the spatial separation between the two clusters resembles Fig. 4 in Stokes et al. (2022), in which the region overlapping with Firn 2 tends to lose mass while the region overlapping with Firn 3 tends to slightly gain mass. Therefore, we infer that this result might indicate that Firn 2 has a less stable condition than Firn 3.

To address the non-linear and complex nature of the relationship between satellite parameters and firn density, we employed an RF regressor model. This model allowed us to incorporate multiple input parameters and handle non-linear relationships effectively. The implementation of the RF regressor successfully reproduced the spatial pattern of the IMAU-FDM density, achieving a low root mean square error (RMSE) of ~~13.38~~14.92 $kg\ m^{-3}$, which outperforms the RMSE of a simple linear model (17.87 $kg\ m^{-3}$). This highlights the potential of using satellite parameters to create a map of long-term mean densities, ~~going beyond the simple reconstruction based on climate drivers as demonstrated by Fraser et al. (2016).~~ matching the conclusion of Fraser et al. (2016), who managed to reconstruct one of the satellite observations (σ^0_A) using climate and firn parameters in the long term.

However, it is important to note some limitations and discrepancies in the RF density map. We observed a slight overestimation of densities in the interior of the Antarctic ice sheet, coupled with an underestimation towards the coastal regions, when compared to the IMAU-FDM densities. This discrepancy may arise from the inability of the RF regressor to extrapolate beyond the training data, leading to the restricted density range in the RF density map (maximum density of $\leq 450\ kg\ m^{-3}$). Furthermore, when comparing the RF and IMAU-FDM densities with the in situ SUMup measurements, we found comparable errors. Similar errors were reported by Keenan et al. (2021), who attributed them to local meteorological phenomena not

captured by climate models and possible measurement uncertainties. These factors, which are not explicitly accounted for in the IMAU-FDM model or the RF regressor trained on that dataset, may contribute to the discrepancies observed.

While the RF regressor successfully captures the spatial variability of the long-term mean density, it falls short in accurately predicting the temporal variation in IMAU-FDM, particularly in coastal regions and megadune areas. Apart from the aforementioned potential underestimation of melt pixels of our clustering method in coastal regions, the temporal discrepancies between the RF regressor and IMAU-FDM can be attributed to the differences in seasonal patterns and the presence of complex climate conditions near the ice shelves. Coastal regions, characterised by ~~low temperature differences between summer and winter, and~~ large negative differences in wind velocity between summer and winter, exhibit larger temporal discrepancies. These findings suggest that IMAU-FDM may not capture the seasonal cycle of fresh snow density in these regions with high wind speeds during winter~~and a relatively small seasonal temperature cycle~~. The simplicity of how the density of freshly fallen snow is calculated within IMAU-FDM, assuming linear dependencies with wind speed and surface temperature (Veldhuijsen et al., 2023), fails to account for the intricate processes involving crystal size, shape, and riming, which are influenced by temperature and wind speed conditions (Judson and Doesken, 2000). The dependence of fresh snow density on wind speed may differ under various temperature conditions, which contributes to the discrepancies observed.

In summary, the RF regressor trained using IMAU-FDM and satellite parameters demonstrates promising results in capturing the spatial pattern of firn density. However, it may not fully capture the temporal fluctuations of IMAU-FDM, primarily due to the dominant influence of surface temperature (represented by T_B) in the RF estimation. The effects of precipitation ~~(e.g., represented by changes in σ^0 Fraser et al., 2016)~~(e.g., represented by changes in σ^0_A Fraser et al., 2016), and wind velocity (e.g., respresented by $PR(f)$ in Champollion et al., 2013) are therefore potentially compromised in the RF model. Additionally, the discrepancy between the meteorological forcing in the IMAU-FDM model and the actual meteorological phenomena can also play a role. The meteorological phenomena can affect the satellite parameters, which in turn influence the RF results, but may not be reflected in the IMAU-FDM output. Our approach of training the RF regressor on IMAU-FDM, which may exhibit spatial and temporal differences compared to actual in situ densities, can therefore be considered a major shortcoming. This limitation should be taken into consideration when interpreting the RF density estimations. Future research could benefit from incorporating more in situ measurements for training the RF regressor, which would improve the accuracy of the temporal density estimates. Furthermore, care should also be taken when using the coarse resolution IMAU-FDM and satellite data to represent the local firn densities. The firn property variation may be small in pixels with relatively flat topography such as Dome C (Picard et al., 2014). However, towards the coastal or mountainous regions, the ability of such coarse resolution to represent firn densities could be compromised, as a mismatch between the local meteorological phenomena, the satellite parameters and the modelled densities can be introduced. Indirect correlations between different layers of firn should also be considered when applying data fusion of multiple microwave frequencies. Additionally, exploring alternative machine learning algorithms or ensemble approaches may further enhance the performance of density estimation and capture the complex relationships between satellite observations and firn density, as assessed by Anilkumar et al. (2023).

Despite the limitations and discrepancies observed, the RF density map generated in this study can serve as an important intermediate step in translating satellite data into density estimations. It provides valuable insights into the discrepancy between

firn models and satellite observations, shedding light on the complexities of the relationship between satellite parameters and firn density. The RF regressor captures the long-term mean density pattern, offering a useful tool for investigating spatial variations in firn density across Antarctica. However, it is essential to exercise caution when interpreting the temporal variations, particularly in coastal regions with complex climate conditions.

Further improvements can be made to enhance the accuracy of the RF regressor in capturing the temporal variations of firn density. This could involve refining the training data and incorporating additional meteorological parameters that influence the satellite observations, as also suggested by Kar and Aksoy (2024). By better accounting for the effects of precipitation and wind velocity on the satellite parameters, the RF regressor could potentially capture a more accurate representation of the temporal dynamics of firn density. Furthermore, advancements in the ~~parameterisation~~ parametrisation of fresh snow density within firn models, considering the complex processes driven by temperature and wind speed conditions, could help bridge the gap between model predictions and satellite observations. Finally, as the performance of the machine learning method varies based on different meteorological phenomena and topography, it can also be recommended for further studies to apply different ~~parameterisations~~ parametrisations for different regions or test other machine learning methods.

6 Conclusions

In conclusion, this study demonstrates the potential of using multiple satellite observations to estimate Antarctic firn densities, with the IMAU-FDM densities serving as a reference. Our findings highlight several key points. Firstly, while satellite observations exhibit a certain level of spatial correlations with firn densities, a consistent linear relationship cannot be established. The correlations between ~~ρ_{12cm}~~ ρ_{40cm} and satellite parameters, particularly T_B, ~~$PR(f)$ and $FR(p)$, indicate their potential influence on firn density variations~~indicate the potential influence of firn density on variations of satellite observations.

Secondly, the impact of firn melt and refreeze on satellite observations is significant. Temporal anomalies in satellite parameters can be adopted to differentiate between wet and dry firn regions. Clustering of satellite observation time series helps to identify melt extents and assess the temporal correlation with densities at the cluster level. Notably, the scattering impact of refrozen melt layers is reflected in prolonged elevated ~~σ^0~~ σ^0_A anomalies. However, in dry snow clusters, the correlation between densities and satellite observations is not evident.

Based on these complexities, a non-linear model, such as the random forest (RF) regressor, is necessary to capture the relationship between firn densities and satellite observations. Our implementation of the RF regressor successfully reproduces the spatial pattern of firn densities, exhibiting good agreement with IMAU-FDM and even outperforming it in certain locations when compared with SUMup density measurements. However, the temporal simulation of densities by the RF regressor is compromised. Individual pixel analyses reveal that the RF densities tend to ~~overestimate densities in summer when they are~~ overlook the inter-annual variations in firn densities when the variations of satellite observations are not in phase with IMAU-FDM densities. In coastal regions, where satellite signals with strong variability dominate, the RF densities are not directly comparable to IMAU-FDM densities. These temporal discrepancies can be attributed to the simplifications in the IMAU-FDM model, particularly in capturing wind and temperature dependencies that strongly influence satellite observations. Furthermore,

limitations of the RF regressor, including the inability to extrapolate from the training dataset and its strong dependence on brightness temperatures, result in a limited range of density estimation and primarily reflect surface temperatures.

Data availability. The SSMIS data are available at https://nsidc.org/data/nsidc-0001/versions/6. The ASCAT Enhanced Resolution Image Products are available at https://www.scp.byu.edu/data/Ascat/SIR/Ascat_sir.html. The SUMup data are available at https://arcticdata.io/catalog/view/doi:10.18739/A2ZS2KD0Z. The ERA5 land hourly data are available at https://doi.org/10.24381/cds.e2161bac. The IMAU-FDM data are available upon request from s.b.m.veldhuijsen@uu.nl.

Appendix A: Temporally averaged satellite parameters and IMAU-FDM density

Figure A1 displays the averaged maps of satellite parameters and ~~ρ_{12cm}~~ρ_{40cm}. This figure aims to demonstrate an overview of the spatial patterns of the data applied in this study. The figure shows that, although all satellite parameters reflect some of the spatial patterns of firn density, none of the parameters shows a spatially consistent relation with ~~ρ_{12cm}~~ρ_{40cm}. For example, in high-elevation regions of East Antarctica, firn densities ~~, $PR(f)$, and $FR(p)$ show similar or reversed broad-scale spatial patterns~~ show similar spatial patterns to T_B and reversed spatial patterns of σ^0_A. However, these patterns are not consistently observed in ~~most coastal regions~~West Antarctica, along the Transantarctic Mountains (location shown in Fig. 2a), and in cluster Firn 5 (Fig. 4), where a significant melt event in 2016 affected the satellite observations (Nicolas et al., 2017).

Appendix B: ~~Comparison between different RF settings~~Time series of clustering results

This appendix section presents the ~~sensitivity analysis introduced in~~ time series of different clusters following Sect. ~~3.3. We assessed the difference between using all satellite parameters ($\boldsymbol{X}$), using T_B and σ^0 only ($\boldsymbol{X_1}$), and using all parameters except for the time series anomalies ($\boldsymbol{X_2}$) as input to the RF regressors. The results of hyperparameter tuning and the assessment metrics are shown in Table **??** and Fig. **??**~~3.2. Figure B1 presents the time series of the mean and 20th–80th percentiles of each parameter for each cluster, (a)–(g) corresponding to clusters 1–7, respectively. Clusters Firn 1–4 exhibit small and short-term variations in T_{Banom} and $\sigma^0 anom$; the extent of variations differ between different clusters. Firn 1 has the smallest variations in T_{Banom} and σ^0_{anom}, which are within ± 5 K and ± 0.25 dB, respectively. ~~Hyperparameter range and optimal values used to specify the random forest (RF) model for different settings (corresponding to Fig. **??**). Hyperparameter Hyperparameter range Value for all parameters Values for T_B and σ^0 Values for T_B, σ^0 and T_B ratios Number of trees 200, 300, 400 400 400 400 Maximum depth of the tree 12, 15, 18 18 18 18 The minimum number of samples at a leaf node 1,~~ Firn 2 and Firn 3 ~~, 5, 7 1 7 1 The number of features to consider when searching for the best split 1, 3, 5, 7 3 1 1 The minimum number of samples to split an internal node~~ have a T_{Banom} between -5 K and 10 K, however, Firn 2 ~~, has~~ a σ^0_{anom} within ± 1 dB, while Firn 3 ~~, has~~ a σ^0_{anom} within ± 0.5 dB. Firn 4 ~~, 5 3 5 2~~ is characterised by a T_{Banom} variation within ± 10 K and a σ^0_{anom} variation within ± 0.5 dB. Finally, the $PR(f)$ and $FR(p)$ time series of Firn 1–4 undergo regular and similar seasonal cycles.

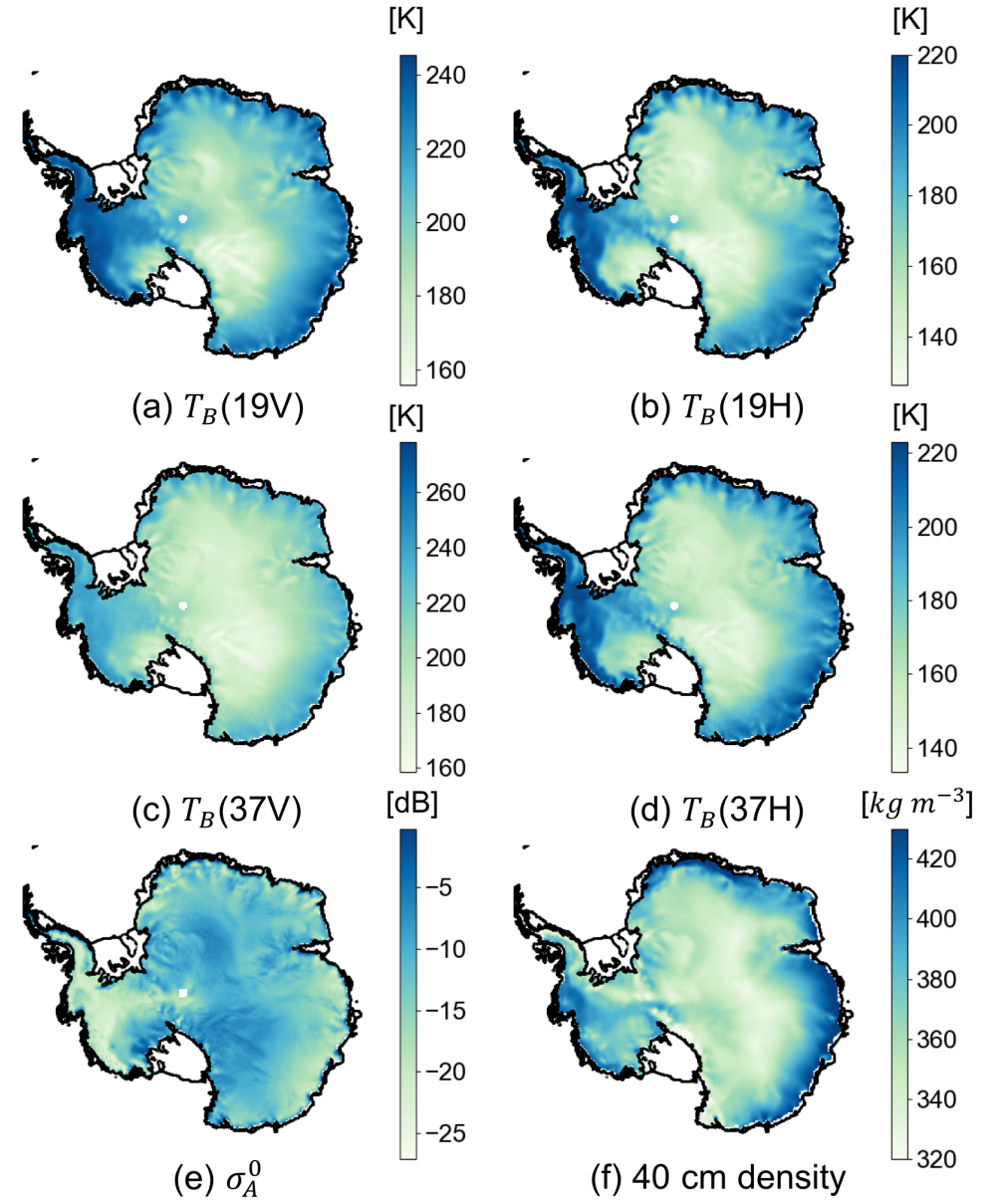

Figure A1. Temporally averaged map of (a) brightness temperature (T_B) from 19 GHz vertical polarisation, (b) T_B from 19 GHz horizontal polarisation, (c) ~~polarisation ratio from 19 GHz ($PR(19\ GHz)$), (d)~~ T_B from 37 GHz vertical polarisation, (ed) T_B from 37 GHz horizontal polarisation, (fe) ~~polarisation ratio from 37 GHz ($PR(37\ GHz)$), (g) frequency ratio from vertical polarisation ($FR(V)$), (h) frequency ratio from vertical polarisation ($FR(H)$), (i)~~ backscatter intensity (σ^0 σ_A^0), and (jf) ~~12~~40 cm IMAU-FDM density (ρ_{12cm} ρ_{40cm}). (a)–(~~h~~d) are acquired or derived parameters from SSMIS, and (~~i~~e) is derived from ASCAT. The coastline is from Depoorter et al. (2013).

~~Figure ?? shows the RMSE and correlation coefficients between~~ On the contrary, clusters Firn 5–7 all show large and abrupt variations in T_{Banom} and σ^0_{anom}, mainly as a result of melt events (e.g., Nicolas et al., 2017) that drastically change absorption, emission and scattering of microwave radiation and thus the T_{Banom} and σ^0_{anom}. The effects of these melt events are also evident in the time series of $PR(f)$, $FR(p)$, and the IMAU-FDM ~~and RF densities when different settings are applied as input to the RF regressors. Generally, the spatial patterns of RMSE and correlation coefficients are similar between all settings. The correlation coefficient using all satellite parameters outperforms the other settings in West Antarctica. The comparison between averages of all metrics indicates that using all satellite parameters slightly outperforms the other settings overall, i.e. lower RMSE and high correlation coefficient. Our interpretation for the observed phenomena is that T_B ratios and time series anomalies theoretically reveal the surface and~~ densities, as the abrupt changes in firn density are associated with the occurrence of melt events (Amory et al., 2024). For example, this can be clearly seen in the time series of cluster Firn 5, where the melt event of 2016 shows a prolonged effect on the σ^0_{anom} time series due to the formation of a sub-surface ~~processes, such as snow metamorphism up to 11 cm depth (Picard et al., 2012). It can be for instance observed that the elevated correlation coefficients in Fig. ??b compared with Fig. ??d and f corresponds to the high grain-index increase (>0.12) in Fig. 4 of Picard et al. (2012) in West Antarctica and Dronning Maud Land (location shown in Fig. 2a). However, we admit that the interpretation should be better supported by in situ measurements, if continuous measurements are available~~refrozen high-density layer in IMAU-FDM. The high-density layer is detected by the scatterometer with stronger snow penetrating capability. In IMAU-FDM, this high density layer appears also in ρ_{40cm} where it increases by approximately $100\ kg\ m^{-3}$. The comparison of all clusters highlights the dominant influence of melt events on T_{Banom} and σ^0_{anom} in the wet-firn pixels, whereas the dry-firn pixels exhibit a more pronounced seasonal variation in satellite parameters. It is important to note that the wet firn clusters are not used in the following RF steps due to the complex impact of the melt–refreeze cycle on satellite observations.

Author contributions. WL and SL designed the study. WL conducted data management, processing and analysis; produced the figures; and provided the manuscript with contributions from all co-authors. SV processed and provided the IMAU-FDM densities. SL provided support on data visualisation and analysis.

Competing interests. Stef Lhermitte is a member of the editorial board of The Cryosphere.

Acknowledgements. Weiran Li is supported by the Dutch Research Council (NWO) on the ALWGO.2017.033 project. Sanne B. M. Veldhuijsen is supported by the Netherlands Organization for Scientific Research (grantno.OCENW.GROOT.2019.091).

We acknowledge National Snow and Ice Data Center (NSIDC) for providing the SSMIS brightness temperature data, Brigham Young University (BYU) Center for Remote Sensing for providing the ASCAT incidence angle normalised backscatter intensity, ECMWF for providing the ERA5 data, and the Surface Mass Balance and Snow on Sea Ice Working Group (SUMup) ~~and the group of Dr Leduc-Leballeur~~ for providing the firn density measurements over Antarctica.

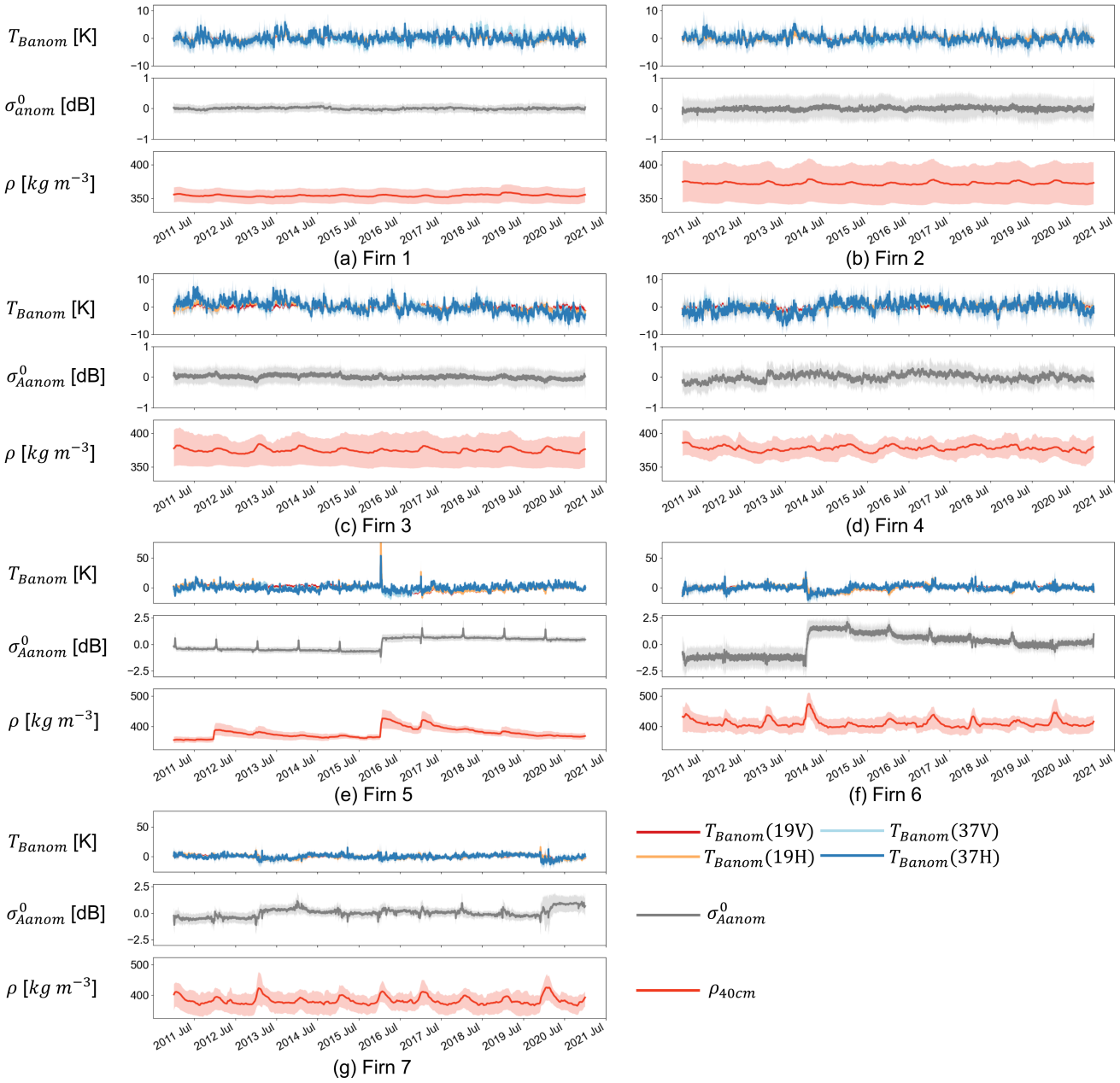

Figure B1. ~~Performance assessment metrics same as~~ Time series of mean (curves) and 20th–80th percentiles (shaded areas) of the clustering results in Fig. ~~7a and b. RMSE and correlation coefficients between IMAU-FDM and RF densities when~~ 4, (a), ~~–~~(~~b~~g) ~~using all satellite parameters (identical~~ corresponding to ~~the settings~~ Snow facies 1–7. The visualised satellite observations are: time series anomalies of ~~this study~~brightness temperature (T_B) from 19 GHz and 37 GHz, both horizontal and vertical polarisation (~~e~~$T_{Banom}(19V)$, $T_{Banom}(19H)$, $T_{Banom}(37V)$ and $T_{Banom}(37H)$, respectively), time series anomalies of backscatter intensity (~~d~~σ^0_{Aanom})~~using T_B and σ^0~~, and IMAU-FDM density at 40 cm (~~e~~ρ_{40cm}) ~~,~~depth. The colours of the curves correspond to the legends in (~~f~~g)~~using all parameters except for T_B and σ^0 anomalies~~.

The authors would also like to thank Pavel Ditmar, Jan Haacker, Sophie de Roda Husman, and Ann-Sofie Zinck for valuable discussions. ChatGPT is used for grammar checks in parts of the manuscript.

References

Amory, C., Buizert, C., Buzzard, S., Case, E., Clerx, N., Culberg, R., Datta, R. T., Dey, R., Drews, R., Dunmire, D., Eayrs, C., Hansen, N., Humbert, A., Kaitheri, A., Keegan, K., Kuipers Munneke, P., Lenaerts, J. T. M., Lhermitte, S., Mair, D., McDowell, I., Mejia, J., Meyer, C. R., Morris, E., Moser, D., Oraschewski, F. M., Pearce, E., de Roda Husman, S., Schlegel, N.-J., Schultz, T., Simonsen, S. B., Stevens, C. M., Thomas, E. R., Thompson-Munson, M., Wever, N., and Wouters, B.: Firn on ice sheets, Nature Reviews Earth & Environment, https://doi.org/10.1038/s43017-023-00507-9, 2024.

Anilkumar, R., Bharti, R., Chutia, D., and Aggarwal, S. P.: Modelling point mass balance for the glaciers of the Central European Alps using machine learning techniques, The Cryosphere, 17, 2811–2828, https://doi.org/10.5194/tc-17-2811-2023, 2023.

Archer, K. J. and Kimes, R. V.: Empirical characterization of random forest variable importance measures, Computational Statistics & Data Analysis, 52, 2249–2260, https://doi.org/10.1016/j.csda.2007.08.015, 2008.

Arndt, S. and Haas, C.: Spatiotemporal variability and decadal trends of snowmelt processes on Antarctic sea ice observed by satellite scatterometers, The Cryosphere, 13, 1943–1958, https://doi.org/10.5194/tc-13-1943-2019, 2019.

Bingham, A. and Drinkwater, M.: Recent changes in the microwave scattering properties of the Antarctic ice sheet, Geoscience and Remote Sensing, IEEE Transactions on, 38, 1810 – 1820, https://doi.org/10.1109/36.851765, 2000.

Breiman, L.: Bagging predictors, Machine Learning, 24, 123–140, https://doi.org/10.1007/bf00058655, 1996.

Breiman, L.: Random Forests, Machine Learning, 45, 5–32, https://doi.org/10.1023/a:1010933404324, 2001.

Brigham Young University (BYU) Microwave Earth Remote Sensing (MERS) laboratory: Standard BYU ASCAT Land/Ice Image Products, https://www.scp.byu.edu/data/Ascat/SIR/Ascat_sir.html, [Access date: Feb. 6, 2021], 2010.

Brucker, L., Picard, G., and Fily, M.: Snow grain-size profiles deduced from microwave snow emissivities in Antarctica, Journal of Glaciology, 56, 514–526, https://doi.org/10.3189/002214310792447806, 2010.

Brucker, L., Picard, G., Arnaud, L., Barnola, J.-M., Schneebeli, M., Brunjail, H., Lefebvre, E., and Fily, M.: Modeling time series of microwave brightness temperature at Dome C, Antarctica, using vertically resolved snow temperature and microstructure measurements, Journal of Glaciology, 57, 171–182, https://doi.org/10.3189/002214311795306736, 2011.

Brucker, L., Dinnat, E. P., Picard, G., and Champollion, N.: Effect of Snow Surface Metamorphism on Aquarius L-Band Radiometer Observations at Dome C, Antarctica, IEEE Transactions on Geoscience and Remote Sensing, 52, 7408–7417, https://doi.org/10.1109/tgrs.2014.2312102, 2014.

Cartwright, J., Fraser, A. D., and Porter-Smith, R.: Polar maps of C-band backscatter parameters from the Advanced Scatterometer, Earth System Science Data, 14, 479–490, https://doi.org/10.5194/essd-14-479-2022, 2022.

Champollion, N., Picard, G., Arnaud, L., Lefebvre, E., and Fily, M.: Hoar crystal development and disappearance at Dome C, Antarctica: observation by near-infrared photography and passive microwave satellite, The Cryosphere, 7, 1247–1262, https://doi.org/10.5194/tc-7-1247-2013, 2013.

Copernicus Climate Change Service: ERA5-Land hourly data from 2001 to present, https://doi.org/10.24381/CDS.E2161BAC, 2019.

Craven, M. and Allison, I.: Firnification and the effects of wind-packing on Antarctic snow, Annals of Glaciology, 27, 239–245, https://doi.org/10.3189/1998aog27-1-239-245, 1998.

de Roda Husman, S., Hu, Z., Wouters, B., Munneke, P. K., Veldhuijsen, S., and Lhermitte, S.: Remote Sensing of Surface Melt on Antarctica: Opportunities and Challenges, IEEE Journal of Selected Topics in Applied Earth Observations and Remote Sensing, pp. 1–20, https://doi.org/10.1109/jstars.2022.3216953, 2022.

Depoorter, M. A., Bamber, J. L., Griggs, J., Lenaerts, J. T. M., Ligtenberg, S. R. M., van den Broeke, M. R., and Moholdt, G.: Synthesized grounding line and ice shelf mask for Antarctica, https://doi.org/10.1594/PANGAEA.819151, supplement to: Depoorter, MA et al. (2013): Calving fluxes and basal melt rates of Antarctic ice shelves. Nature, 502, 89-92, https://doi.org/10.1038/nature12567, 2013.

Early, D. and Long, D.: Image reconstruction and enhanced resolution imaging from irregular samples, IEEE Transactions on Geoscience and Remote Sensing, 39, 291–302, https://doi.org/10.1109/36.905237, 2001.

Fahnestock, M., Bindschadler, R., Kwok, R., and Jezek, K.: Greenland Ice Sheet Surface Properties and Ice Dynamics from ERS-1 SAR Imagery, Science, 262, 1530–1534, https://doi.org/10.1126/science.262.5139.1530, 1993.

Fahnestock, M. A., Scambos, T. A., Shuman, C. A., Arthern, R. J., Winebrenner, D. P., and Kwok, R.: Snow megadune fields on the East Antarctic Plateau: Extreme atmosphere-ice interaction, Geophysical Research Letters, 27, 3719–3722, https://doi.org/10.1029/1999gl011248, 2000.

Figa-Saldaña, J., Wilson, J. J., Attema, E., Gelsthorpe, R., Drinkwater, M. R., and Stoffelen, A.: The advanced scatterometer (ASCAT) on the meteorological operational (MetOp) platform: A follow on for European wind scatterometers, Canadian Journal of Remote Sensing, 28, 404–412, https://doi.org/10.5589/m02-035, 2002.

Fraser, A. D., Nigro, M. A., Ligtenberg, S. R. M., Legrésy, B., Inoue, M., Cassano, J. J., Kuipers Munneke, P., Lenaerts, J. T. M., Young, N. W., Treverrow, A., van den Broeke, M., and Enomoto, H.: Drivers of ASCAT C band backscatter variability in the dry snow zone of Antarctica, Journal of Glaciology, 62, 170–184, https://doi.org/10.1017/jog.2016.29, 2016.

Fujita, S., Goto-Azuma, K., Hirabayashi, M., Hori, A., Iizuka, Y., Motizuki, Y., Motoyama, H., and Takahashi, K.: Densification of layered firn in the ice sheet at Dome Fuji, Antarctica, Journal of Glaciology, 62, 103–123, https://doi.org/10.1017/jog.2016.16, 2016.

Hastie, T., Tibshirani, R., and Friedman, J.: Random Forests, pp. 587–604, Springer New York, https://doi.org/10.1007/978-0-387-84858-7_15, 2008.

Hengl, T., Nussbaum, M., Wright, M. N., Heuvelink, G. B., and Gräler, B.: Random forest as a generic framework for predictive modeling of spatial and spatio-temporal variables, PeerJ, 6, e5518, https://doi.org/10.7717/peerj.5518, 2018.

Johnson, A., Fahnestock, M., and Hock, R.: Evaluation of passive microwave melt detection methods on Antarctic Peninsula ice shelves using time series of Sentinel-1 SAR, Remote Sensing of Environment, 250, 112 044, https://doi.org/https://doi.org/10.1016/j.rse.2020.112044, 2020.

Judson, A. and Doesken, N.: Density of Freshly Fallen Snow in the Central Rocky Mountains, Bulletin of the American Meteorological Society, 81, 1577–1587, https://doi.org/10.1175/1520-0477(2000)081<1577:doffsi>2.3.co;2, 2000.

Kar, R. and Aksoy, M.: Passive Microwave Remote Sensing of the Antarctic Ice Sheet: Retrieval of Firn Properties Near the Concordia Station, IEEE Geoscience and Remote Sensing Letters, 21, 1–5, https://doi.org/10.1109/lgrs.2023.3343594, 2024.

Keenan, E., Wever, N., Dattler, M., Lenaerts, J. T. M., Medley, B., Munneke, P. K., and Reijmer, C.: Physics-based SNOWPACK model improves representation of near-surface Antarctic snow and firn density, The Cryosphere, 15, 1065–1085, https://doi.org/10.5194/tc-15-1065-2021, 2021.

Kingslake, J., Ely, J. C., Das, I., and Bell, R. E.: Widespread movement of meltwater onto and across Antarctic ice shelves, Nature, 544, 349–352, https://doi.org/10.1038/nature22049, 2017.

Koenig, L. and Montgomery, L.: Surface Mass Balance and Snow Depth on Sea Ice Working Group (SUMup) snow density subdataset, Greenland and Antartica, 1950-2018, https://doi.org/10.18739/A2JH3D23R, 2018.

Kuipers Munneke, P., Ligtenberg, S. R. M., Noël, B. P. Y., Howat, I. M., Box, J. E., Mosley-Thompson, E., McConnell, J. R., Steffen, K., Harper, J. T., Das, S. B., and van den Broeke, M. R.: Elevation change of the Greenland Ice Sheet due to surface mass balance and firn processes, 1960–2014, The Cryosphere, 9, 2009–2025, https://doi.org/10.5194/tc-9-2009-2015, 2015.

Kunkee, D. B., Poe, G. A., Boucher, D. J., Swadley, S. D., Hong, Y., Wessel, J. E., and Uliana, E. A.: Design and Evaluation of the First Special Sensor Microwave Imager/Sounder, IEEE Transactions on Geoscience and Remote Sensing, 46, 863–883, https://doi.org/10.1109/tgrs.2008.917980, 2008.

Leduc-Leballeur, M., Picard, G., Macelloni, G., Arnaud, L., Brogioni, M., Mialon, A., and Kerr, Y.: Influence of snow surface properties on L-band brightness temperature at Dome C, Antarctica, Remote Sensing of Environment, 199, 427–436, https://doi.org/https://doi.org/10.1016/j.rse.2017.07.035, 2017.

Leduc-Leballeur, M., Picard, G., Macelloni, G., Arnaud, L., Brogioni, M., Mialon, A., and Kerr, Y. H.: Snow density at Dome C, Antarctica in 2015, https://doi.org/10.1594/PANGAEA.934373, [Access date: Jun. 7, 2022], 2021.

Lehning, M., Bartelt, P., Brown, B., Fierz, C., and Satyawali, P.: A physical SNOWPACK model for the Swiss avalanche warning: Part II. Snow microstructure, Cold Regions Science and Technology, 35, 147–167, https://doi.org/10.1016/s0165-232x(02)00073-3, 2002.

Lenaerts, J. T. M., Lhermitte, S., Drews, R., Ligtenberg, S. R. M., Berger, S., Helm, V., Smeets, C. J. P. P., van den Broeke, M. R., van de Berg, W. J., van Meijgaard, E., Eijkelboom, M., Eisen, O., and Pattyn, F.: Meltwater produced by wind–albedo interaction stored in an East Antarctic ice shelf, Nature Climate Change, 7, 58–62, https://doi.org/10.1038/nclimate3180, 2016.

Li, J. and Zwally, H. J.: Modeling the density variation in the shallow firn layer, Annals of Glaciology, 38, 309–313, https://doi.org/10.3189/172756404781814988, 2004.

Li, W., Lhermitte, S., and López-Dekker, P.: The potential of synthetic aperture radar interferometry for assessing meltwater lake dynamics on Antarctic ice shelves, The Cryosphere, 15, 5309–5322, https://doi.org/10.5194/tc-15-5309-2021, 2021.

Ligtenberg, S. R. M., Helsen, M. M., and van den Broeke, M. R.: An improved semi-empirical model for the densification of Antarctic firn, The Cryosphere, 5, 809–819, https://doi.org/10.5194/tc-5-809-2011, 2011.

Lindsley, R. D. and Long, D. G.: Standard BYU ASCAT Land/Ice Image Products, Tech. rep., Brigham Young University Microwave Earth Remote Sensing (MERS) Laboratory, https://www.scp.byu.edu/docs/pdf/MERS1002.pdf, [Access date: Jun. 20, 2022], 2010.

Long, D. and Drinkwater, M.: Azimuth variation in microwave scatterometer and radiometer data over Antarctica, IEEE Transactions on Geoscience and Remote Sensing, 38, 1857–1870, https://doi.org/10.1109/36.851769, 2000.

Long, D., Hardin, P., and Whiting, P.: Resolution enhancement of spaceborne scatterometer data, IEEE Transactions on Geoscience and Remote Sensing, 31, 700–715, https://doi.org/10.1109/36.225536, 1993.

Macelloni, G., Brogioni, M., Pampaloni, P., and Cagnati, A.: Multifrequency Microwave Emission From the Dome-C Area on the East Antarctic Plateau: Temporal and Spatial Variability, IEEE Transactions on Geoscience and Remote Sensing, 45, 2029–2039, https://doi.org/10.1109/tgrs.2007.890805, 2007.

Meier, W. N., Stewart, J. S., Wilcox, H., Scott, D. J., and Hardman, M. A.: DMSP SSM/I-SSMIS Daily Polar Gridded Brightness Temperatures, Boulder, Colorado USA. NASA National Snow and Ice Data Center Distributed Active Archive Center, https://doi.org/10.5067/MXJL42WSXTS1, [Date Accessed: Mar. 15, 2021], 2021.

Meredith, M., Sommerkorn, M., Cassotta, S., Derksen, C., Ekaykin, A., Hollowed, A., Kofinas, G., Mackintosh, A., Melbourne-Thomas, J., Muelbert, M., Ottersen, G., Pritchard, H., and Schuur, E.: Polar Regions, chap. 3, pp. 203–320, Cambridge University Press, Cambridge, UK and New York, NY, USA, https://doi.org/10.1017/9781009157964.005, 2019.

Montgomery, L., Koenig, L., and Alexander, P.: The SUMup dataset: compiled measurements of surface mass balance components over ice sheets and sea ice with analysis over Greenland, Earth System Science Data, 10, 1959–1985, https://doi.org/10.5194/essd-10-1959-2018, 2018.

Nicolas, J. P., Vogelmann, A. M., Scott, R. C., Wilson, A. B., Cadeddu, M. P., Bromwich, D. H., Verlinde, J., Lubin, D., Russell, L. M., Jenkinson, C., Powers, H. H., Ryczek, M., Stone, G., and Wille, J. D.: January 2016 extensive summer melt in West Antarctica favoured by strong El Niño, Nature Communications, 8, https://doi.org/10.1038/ncomms15799, 2017.

Pattyn, F. and Morlighem, M.: The uncertain future of the Antarctic Ice Sheet, Science, 367, 1331–1335, https://doi.org/10.1126/science.aaz5487, 2020.

Picard, G., Fily, M., and Gallee, H.: Surface melting derived from microwave radiometers: a climatic indicator in Antarctica, Annals of Glaciology, 46, 29–34, https://doi.org/10.3189/172756407782871684, 2007.

Picard, G., Brucker, L., Fily, M., Gallée, H., and Krinner, G.: Modeling time series of microwave brightness temperature in Antarctica, Journal of Glaciology, 55, 537–551, https://doi.org/10.3189/002214309788816678, 2009.

Picard, G., Domine, F., Krinner, G., Arnaud, L., and Lefebvre, E.: Inhibition of the positive snow-albedo feedback by precipitation in interior Antarctica, Nature Climate Change, 2, 795–798, https://doi.org/10.1038/nclimate1590, 2012.

Picard, G., Royer, A., Arnaud, L., and Fily, M.: Influence of meter-scale wind-formed features on the variability of the microwave brightness temperature around Dome C in Antarctica, The Cryosphere, 8, 1105–1119, https://doi.org/10.5194/tc-8-1105-2014, 2014.

Rignot, E.: Mass balance of East Antarctic glaciers and ice shelves from satellite data, Annals of Glaciology, 34, 217–227, https://doi.org/10.3189/172756402781817419, 2002.

Rizzoli, P., Martone, M., Rott, H., and Moreira, A.: Characterization of Snow Facies on the Greenland Ice Sheet Observed by TanDEM-X Interferometric SAR Data, Remote Sensing, 9, https://doi.org/10.3390/rs9040315, 2017.

Sandri, M. and Zuccolotto, P.: Analysis and correction of bias in Total Decrease in Node Impurity measures for tree-based algorithms, Statistics and Computing, 20, 393–407, https://doi.org/10.1007/s11222-009-9132-0, 2009.

Schröder, L., Horwath, M., Dietrich, R., Helm, V., van den Broeke, M. R., and Ligtenberg, S. R. M.: Four decades of Antarctic surface elevation changes from multi-mission satellite altimetry, The Cryosphere, 13, 427–449, https://doi.org/10.5194/tc-13-427-2019, 2019.

Spergel, J. J., Kingslake, J., Creyts, T., van Wessem, M., and Fricker, H. A.: Surface meltwater drainage and ponding on Amery Ice Shelf, East Antarctica, 1973–2019, Journal of Glaciology, p. 1–14, https://doi.org/10.1017/jog.2021.46, 2021.

Stiles, W. H. and Ulaby, F. T.: The active and passive microwave response to snow parameters: 1. Wetness, Journal of Geophysical Research: Oceans, 85, 1037–1044, https://doi.org/10.1029/jc085ic02p01037, 1980.

Stokes, C. R., Abram, N. J., Bentley, M. J., Edwards, T. L., England, M. H., Foppert, A., Jamieson, S. S. R., Jones, R. S., King, M. A., Lenaerts, J. T. M., Medley, B., Miles, B. W. J., Paxman, G. J. G., Ritz, C., van de Flierdt, T., and Whitehouse, P. L.: Response of the East Antarctic Ice Sheet to past and future climate change, Nature, 608, 275–286, https://doi.org/10.1038/s41586-022-04946-0, 2022.

Strobl, C., Boulesteix, A.-L., and Augustin, T.: Unbiased split selection for classification trees based on the Gini Index, Computational Statistics & Data Analysis, 52, 483–501, https://doi.org/10.1016/j.csda.2006.12.030, 2007.

Sugiyama, S., Enomoto, H., Fujita, S., Fukui, K., Nakazawa, F., Holmlund, P., and Surdyk, S.: Snow density along the route traversed by the Japanese-Swedish Antarctic Expedition 2007/08, Journal of Glaciology, 58, 529–539, https://doi.org/10.3189/2012jog11j201, 2012.

Surdyk, S.: Using microwave brightness temperature to detect short-term surface air temperature changes in Antarctica: An analytical approach, Remote Sensing of Environment, 80, 256–271, https://doi.org/10.1016/s0034-4257(01)00308-x, 2002.

Tedesco, M.: Snowmelt detection over the Greenland ice sheet from SSM/I brightness temperature daily variations, Geophysical Research Letters, 34, https://doi.org/10.1029/2006gl028466, 2007.

Tedesco, M.: Assessment and development of snowmelt retrieval algorithms over Antarctica from K-band spaceborne brightness temperature (1979–2008), Remote Sensing of Environment, 113, 979–997, https://doi.org/10.1016/j.rse.2009.01.009, 2009.

Tedesco, M. and Kim, E.: Retrieval of dry-snow parameters from microwave radiometric data using a dense-medium model and genetic algorithms, IEEE Transactions on Geoscience and Remote Sensing, 44, 2143–2151, https://doi.org/10.1109/tgrs.2006.872087, 2006.

Tran, N., Remy, F., Feng, H., and Femenias, P.: Snow Facies Over Ice Sheets Derived From Envisat Active and Passive Observations, IEEE Transactions on Geoscience and Remote Sensing, 46, 3694–3708, https://doi.org/10.1109/tgrs.2008.2000818, 2008.

Trusel, L. D., Frey, K. E., and Das, S. B.: Antarctic surface melting dynamics: Enhanced perspectives from radar scatterometer data, Journal of Geophysical Research: Earth Surface, 117, n/a–n/a, https://doi.org/10.1029/2011jf002126, 2012.

Ulaby, F., Siquera, P., Nashashibi, A., and Sarabandi, K.: Semi-empirical model for radar backscatter from snow at 35 and 95 GHz, IEEE Transactions on Geoscience and Remote Sensing, 34, 1059–1065, https://doi.org/10.1109/36.536521, 1996.

Vafakhah, M., Nasiri Khiavi, A., Janizadeh, S., and Ganjkhanlo, H.: Evaluating different machine learning algorithms for snow water equivalent prediction, Earth Science Informatics, 15, 2431–2445, https://doi.org/10.1007/s12145-022-00846-z, 2022.

van den Broeke, M.: Depth and Density of the Antarctic Firn Layer, Arctic, Antarctic, and Alpine Research, 40, 432–438, https://doi.org/10.1657/1523-0430(07-021)[broeke]2.0.co;2, 2008.

van den Broeke, M. R., Winther, J.-G., Isaksson, E., Pinglot, J. F., Karlöf, L., Eiken, T., and Conrads, L.: Climate variables along a traverse line in Dronning Maud Land, East Antarctica, Journal of Glaciology, 45, 295–302, https://doi.org/10.3189/s0022143000001799, 1999.

van Wessem, J. M., van de Berg, W. J., Noël, B. P. Y., van Meijgaard, E., Amory, C., Birnbaum, G., Jakobs, C. L., Krüger, K., Lenaerts, J. T. M., Lhermitte, S., Ligtenberg, S. R. M., Medley, B., Reijmer, C. H., van Tricht, K., Trusel, L. D., van Ulft, L. H., Wouters, B., Wuite, J., and van den Broeke, M. R.: Modelling the climate and surface mass balance of polar ice sheets using RACMO2 – Part 2: Antarctica (1979–2016), The Cryosphere, 12, 1479–1498, https://doi.org/10.5194/tc-12-1479-2018, 2018.

Veldhuijsen, S. B. M., van de Berg, W. J., Brils, M., Munneke, P. K., and van den Broeke, M. R.: Characteristics of the 1979–2020 Antarctic firn layer simulated with IMAU-FDM v1.2A, The Cryosphere, 17, 1675–1696, https://doi.org/10.5194/tc-17-1675-2023, 2023.

Verjans, V., Leeson, A. A., Nemeth, C., Stevens, C. M., Kuipers Munneke, P., Noël, B., and van Wessem, J. M.: Bayesian calibration of firn densification models, The Cryosphere, 14, 3017–3032, https://doi.org/10.5194/tc-14-3017-2020, 2020.

Viallon-Galinier, L., Hagenmuller, P., and Eckert, N.: Combining modelled snowpack stability with machine learning to predict avalanche activity, The Cryosphere, 17, 2245–2260, https://doi.org/10.5194/tc-17-2245-2023, 2023.

Ward, Jr., J. H.: Hierarchical Grouping to Optimize an Objective Function, Journal of the American Statistical Association, 58, 236–244, https://doi.org/10.1080/01621459.1963.10500845, 1963.

Zwally, H. J., Giovinetto, M. B., Li, J., Cornejo, H. G., Beckley, M. A., Brenner, A. C., Saba, J. L., and Yi, D.: Mass changes of the Greenland and Antarctic ice sheets and shelves and contributions to sea-level rise: 1992–2002, Journal of Glaciology, 51, 509–527, https://doi.org/10.3189/172756505781829007, 2005.